Quantification of seasonal and diurnal dynamics of subglacial channels using seismic observations on an Alpine Glacier.

Ugo Nanni[1], Florent Gimbert[1], Christian Vincent[1], Dominik Gräff[2], Fabian Walter[2], Luc Piard[1], and Luc Moreau[3]

[1]University of Grenoble Alpes, CNRS, IRD, IGE, Grenoble, France
[2]Laboratory of Hydraulics, Hydrology and Glaciology (VAW), ETH Zürich, Zürich, Switzerland,
[3]Edytem, CNRS, Université de Savoie, Chambéry, France

Correspondence: Ugo Nanni (ugo.nanni@univ-grenoble-alpes.fr)

Abstract. Water flowing below glaciers exerts a major control on glacier basal sliding. However, our knowledge of the physics of subglacial hydrology and its link with sliding is limited because of lacking observations. Here we use a two-year long dataset made of on-ice measured seismic and in-situ measured glacier basal sliding speed on Glacier d'Argentière (French Alps) to investigate the physics of subglacial channels and its potential link with glacier basal sliding. Using dedicated theory and concomitant measurements of water discharge, we quantify temporal changes in channels hydraulic radius and hydraulic pressure gradient. At seasonal timescales we find that hydraulic radius and hydraulic pressure gradient respectively exhibit two- and six-fold increase from spring to summer, followed by comparable decrease towards autumn. At low discharge during the early and late melt season channels respond to changes in discharge mainly through changes in hydraulic radius, a regime that is consistent with predictions of channels behaving at equilibrium. In contrast, at high discharge and high short-term water-supply variability (summertime), channels undergo strong changes in hydraulic pressure gradient, a behavior that is consistent with channels behaving out-of-equilibrium. This out-of-equilibrium regime is further supported by observations at the diurnal scale, which support that channels pressurize in the morning and depressurize in the afternoon. During summer we also observe high and sustained basal sliding speed, which supports that the widespread inefficient drainage system (cavities) is likely pressurized concomitantly with the channel-system. We propose that pressurized channels help sustain high pressure in cavities (and therefore high glacier sliding speed) through an efficient hydraulic connection between the two systems. The present findings provide an essential basis for testing the physics represented in subglacial hydrology and glacier sliding models.

1 Introduction

Subglacial water flow exerts a major control on glacier and ice sheet dynamics and their response to variations in water supply (e.g. Iken and Truffe, 1997; Zwally et al., 2002; Sundal et al., 2011; Bartholomaus et al., 2011; Chandler et al., 2013; Hewitt, 2013; Brondex et al., 2017; Joughin et al., 2018). Water flowing at the base of glaciers modulates glacier basal sliding by lubricating the ice-bed interface. The higher the water pressure the weaker the basal friction, resulting in faster glacier sliding (Iken and Bindschadler, 1986; Schoof, 2005; Gagliardini et al., 2007). Water pressure does not simply depend on the total

water input but also on the way the water is conveyed through the subglacial drainage system (Lliboutry, 1968), a system that has, yet, yielded limited observations (Flowers, 2015).

The subglacial drainage system of hard-bedded glaciers is considered to be two-fold. First, cavities form on the downstream lee of bedrock bumps and are thought to enhance basal sliding through reducing the apparent bed roughness (Lliboutry, 1968). These cavities constitute a widespread inefficient drainage system associated with high basal water pressure, slow water flow (of the order of 10^{-2} m.s^{-1}, see e.g. Richards et al. (1996)) and limited hydraulic conductivity. Second, subglacial channels form into the ice from conduit melt by flowing water heat dissipation, and close through ice creep (Röthlisberger, 1972; Nye, 1976). These channels constitute a localized efficient drainage system associated with lower basal water pressure, faster water flow and higher hydraulic conductivity compared to within cavities. A drainage system for which a steady water input is routed through channels tends to slow basal sliding compared to if water is predominantly routed through cavities (e.g. Fountain and Walder, 1998; Schoof, 2010). Most of the current subglacial drainage models (Schoof, 2010; Hewitt, 2013; Werder et al., 2013; Gagliardini and Werder, 2018) are based on this two-fold representation. These models succeed in capturing the two-way channel-cavity coupling but still strongly rely on the choice of model parameters (e.g. cavities and channels hydraulic conductivity, channels opening and closing rates, see de Fleurian et al., 2018). Observational constraints on these parameters (e.g. water pressure, channel properties) and on the channel-cavity-sliding link are however very limited because of the limited observations of the drainage system and concomitant measurements of basal sliding speed (Flowers, 2015; de Fleurian et al., 2018).

Direct observations of the drainage system on temperate glaciers have been relying on the analysis of water discharge measured near glacier outlets (Collins, 1979; Hooke et al., 1985; Tranter et al., 1996, 1997; Anderson et al., 2003; Theakstone and Knudsen, 1989; Chandler et al., 2013), of dye tracing experiments (Seaberg et al., 1988; Willis et al., 1990; Nienow et al., 1996, 1998), of recently exposed subglacial environments (Vivian and Bocquet, 1973; Walder and Hallet, 1979), of local water pressure boreholes measurements (Hantz and Lliboutry, 1983; Copland et al., 1997; Sugiyama et al., 2011; Andrews et al., 2014; Hoffman et al., 2016; Rada and Schoof, 2018; Gräff et al., 2019) or of radar measurements (Church et al., 2019). These methods are mostly point-scale and often focus on the cavity-system due to the very narrow extent of the channel-system (Rada and Schoof, 2018). As a consequence, quantitative information on channels' long term temporal dynamics is limited, such that channels' properties (e.g. size, water flow velocity) and dynamics (e.g. opening and closure rate) remain poorly constrained.

Interactions between channels and cavities are often inferred from evaluating glacier flow-velocity variations in response to meltwater supply variability. High and sustained water supply over monthly timescales (e.g. during the peak melt season) has been linked to glacier deceleration (Bartholomew et al., 2010; Sole et al., 2013; Tedstone et al., 2013, 2015). This behavior is related to the fact that channels-development increases the drainage system capacity and is, therefore, expected to reduce the average basal water pressure (Fountain and Walder, 1998). On the contrary, during short term water supply increase (e.g. at the early melt season or at diurnal scales), glacier velocity changes have been observed to occur concomitantly with wa-

ter supply changes (Parizek and Alley, 2004; Palmer et al., 2011; Sole et al., 2013; Doyle et al., 2014; Vincent and Moreau, 2016). This behavior is mostly related to the pressurization of the cavity-system, causing average basal water pressure rise and subsequent basal sliding speed increase (e.g. Nienow et al., 2005; Schoof, 2010; Rada and Schoof, 2018). During periods of well-developed channelized system (e.g. in summer), this behavior has also been observed because of a channelized system drainage capacity being overwhelmed by the water input changes (Bartholomaus et al., 2008; Andrews et al., 2014) causing pressurized channel flow. These studies have been capable to underline the overall differences between cavity and channel control on subglacial water pressure over different timescales. However, the lack of dedicated channels observations independent of those on cavities and concomitant with glacier sliding speed measurements renders difficult a more quantitative characterization of the physics of subglacial hydrology and its link with sliding.

Here we use on-ice seismology to explore the evolution of subglacial channels over two complete melt seasons. Over the last decade an increasing number of studies have shown the high potential of analyzing high-frequency (>1 Hz) ambient seismic noise to investigate turbulent water flow and sediment transport in terrestrial rivers and streams (e.g. Burtin et al., 2008, 2011; Tsai et al., 2012; Schmandt et al., 2013; Gimbert et al., 2014). The recent work of Gimbert et al. (2016) based on observations of Bartholomaus et al. (2015) suggests that passive seismology may help filling the observational gap on the physics of subglacial channels. Gimbert et al. (2016) adapted to subglacial channels a physical framework that describes how turbulent water flow generates seismic waves and that was initially developed for rivers by Gimbert et al. (2014). Contrary to rivers, subglacial channels have the capability to be full and thus to undergo pressurized situations. By applying this modified framework to the Mendenhall glacier (Alaska) over a two-month long summer period, the authors demonstrate that one can use concomitant seismic noise and water discharge measurements to continuously and separately quantify relative changes in channel hydraulic pressure gradient and channel hydraulic radius. They inferred that channels mainly evolve through changes in hydraulic radius over long time scales (multi-weekly), whereas changes in hydraulic pressure gradient are often short-lived (sub-daily to weekly). The use of such an approach to investigate channel physics on relevant glaciological timescales (e.g. diurnal and seasonal) yet remains to be conducted, and the resulting channels properties remain to be compared to other independent observations, such as basal sliding speed. This is the objective of our study.

We conduct a unique and almost uninterrupted two-years passive seismic survey on Glacier d'Argentière (French Alps), together with continuous measurements of subglacial water discharge, glacier basal sliding speed and local subglacial water pressure. First, we characterize the subglacial channel-flow-induced seismic power signature and use the model of Gimbert et al. (2016) to derive timeseries of hydraulic pressure gradient and hydraulic radius. We then compare these channel properties to the other independent measurements of glacier sliding speed and basal water pressure. We also compare our seismically-derived observations with the theory for subglacial channels physics proposed by Röthlisberger (1972) to assess the implications of these analysis for channels physics. Finally, we investigate the equilibrium state of subglacial channels to discuss the channel-cavity interactions and their potential link with basal sliding throughout the melt season. Doing so will also allow us

to discuss the applicability of such an approach to improve our general knowledge on subglacial hydrology mechanisms of mountain glaciers and ice sheets.

2 Rational

Here we provide a brief background on the theoretical framework of Gimbert et al. (2016), which relates seismic noise and water discharge to subglacial channel-flow properties, and that of Röthlisberger (1972), which predicts subglacial channel hydraulic pressure gradient and hydraulic radius scaling as a function of water discharge under certain assumptions. Refer to table C1 in Appendix C for a summary of all variables, physical quantities, and mathematical functions defined in the following sections.

2.1 Theory of subglacial channel-flow-induced seismic noise

Turbulent water flow in a river or a subglacial channel generates frictional forces F acting on the near boundaries (e.g. river bed or conduit wall), which in turn cause seismic waves with given amplitude and spectral signature (Gimbert et al., 2014). By propagating through a medium (e.g. rock, gravel or ice), seismic waves cause ground motion at any location x away from the source location x_0 (Fig. 1). The relationship between the force timeseries $F(t, x_0)$ applied at x_0 in a channel and the ground velocity timeseries $U(t, x)$ measured at x can be described from Aki and Richards (2002) as

$$U(t, x) = F(t, x_0) \otimes \frac{dG(t, x; x_0)}{dt}, \tag{1}$$

where $G(t)$ is the displacement Green's function that converts the force applied at x_0 into ground displacement at x and the notation $\otimes$ stands for the convolution operator. The seismic power P of such signal is defined over a time period T as

$$P(f, x) = \frac{U(f, x)^2}{T}. \tag{2}$$

where $U(f) = \mathcal{F}(U(t))$ is the Fourier transform of the ground velocity timeseries and f is the frequency. We note P_w the seismic power induced by turbulent water flow. Based on a description of the force $F(f)$ as a function of flow parameters, Gimbert et al. (2014) demonstrated that P_w scales as

$$P_w(f) \propto \zeta(\frac{H}{k_s}) W u_*^{14/3} \tag{3}$$

where u_* is river wall shear velocity, W is river width and ζ is a function that accounts for turbulence intensity changes with changes in the apparent roughness that depends on H the flow depth and k_s the wall roughness size (Fig. 1).
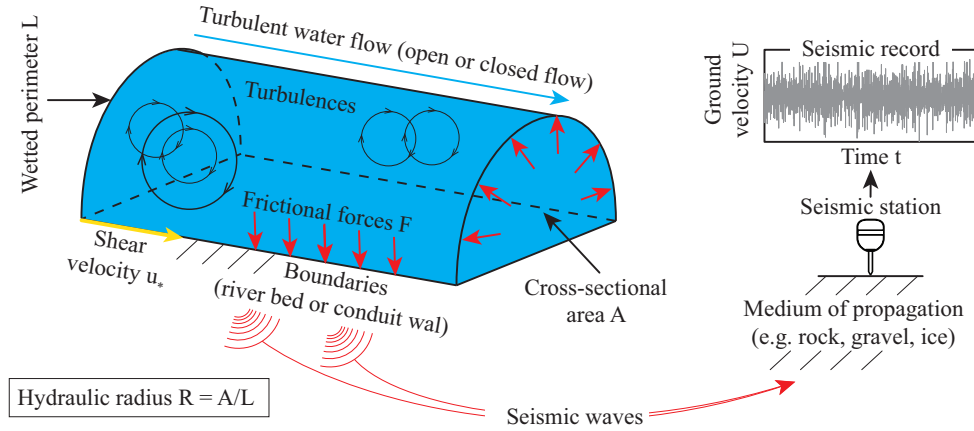
Figure 1. Schematic representation of subglacial channel-flow-induced seismic noise. Representation of an idealized conduit of hydraulic radius R with a wall shear velocity u_* (see Eq.(3)). Turbulent flow generates frictional forces F causing seismic waves and resulting in a ground velocity U that is recorded at a distant seismic station (see Eq.(1)).

To relate P_w to subglacial channels properties, Gimbert et al. (2016) expressed the shear velocity as $u_* = \sqrt{gRS}$ where g is gravitational acceleration, R the hydraulic radius and S the hydraulic pressure gradient. The hydraulic radius R is defined as the ratio of the cross-sectional area of the channel flow to its wet perimeter (Fig. 1). This parameter scales with flow depth for open channel-flow. The hydraulic pressure gradient S is a function of both the water pressure rate of change in the flow direction and the bed slope. For free surface flow S equals channel slope. In a case of constant channel slope and channel geometry, increasing S means closed and pressurizing channel-flow.

Gimbert et al. (2016) then expressed water discharge Q as a function of water flow velocity V_w using the Manning-Strickler relation $V_w = \frac{R^{2/3}S^{1/2}}{n'}$ with n' is the Manning's coefficient (Manning et al., 1890; Strickler, 1981). To study P_w for a subglacial channel flow configuration, Gimbert et al. (2016) considered that the source-to-station distance is constant, such that changes in P_w are not caused by changes in source (channel) position. Gimbert et al. (2016) then assumed a constant number N of channels and thus neglected the dependency of P_w on N. Here we include the dependency of P_w on N by considering that all channels have equal hydraulic radius and hydraulic pressure gradient (i.e. are of similar size and position compared to the seismic station) such that

$$P_w \propto N\beta R^{14/3}S^{7/3} \tag{4}$$

$$Q \propto N\beta R^{8/3}S^{1/2}, \tag{5}$$

where β is a function of conduit shape and fullness that may be neglected (see supporting materials of Gimbert et al. (2016) for details). Combining Eqs.(4) and (5) and neglecting changes in β leads to the two following formulations for P_w,

$$P_w \propto R^{-82/9}Q^{14/3}N^{-11/3} \tag{6}$$
$$P_w \propto S^{41/24}Q^{5/4}N^{-1/4}. \tag{7}$$

From Eqs.(6) and (7) two end-member cases can be evaluated. If changes in discharge occur at constant channel geometry (i.e. constant R and N) from Eq.(6) we have

$$P_w \propto Q^{14/3}, \tag{8}$$

In contrast, if changes in discharge occur at constant hydraulic pressure gradient and channel number (regardless of whether the conduit is full or not) from Eq.(7) we have

$$P_w \propto Q^{5/4}. \tag{9}$$

Beyond these end-member scenarii, one can use measurements of P_w and Q to invert for relative changes in R and S using Eqs.(6) and (7) as:

$$S = S_{ref}\left(\frac{P_w}{P_{w,ref}}\right)^{24/41}\left(\frac{Q}{Q_{ref}}\right)^{-30/41}\left(\frac{N}{N_{ref}}\right)^{6/41}, \tag{10}$$
$$R = R_{ref}\left(\frac{P_w}{P_{w,ref}}\right)^{-9/82}\left(\frac{Q}{Q_{ref}}\right)^{21/41}\left(\frac{N}{N_{ref}}\right)^{-33/82}, \tag{11}$$

where the subset *ref* stands for a reference state, which has to be defined over the same time period for both Q and P_w, but not necessarily for R and S. Details on the derivation from Eqs.(6) and (7) to Eqs.(10) and (11) can be found in Gimbert et al. (2016). In the following we consider N as constant to invert for R and S, and later we support that our inversions are not significantly biased by potential changes in N (Sect. 6.1).

2.2 R-channels theory

To date, state-of-the art subglacial drainage models use the theories of Röthlisberger (1972) to describe subglacial channel dynamics (see de Fleurian et al. (2018) for model inter-comparisons). Channels described in these theories are assumed to be of semi-circular shape and to form into the ice through melt by heat dissipation from the flowing water and close through ice

creep. A channel evolves at steady state with water discharge Q if melt and creep rates change instantaneously with changes in Q. A steady-state channel is at equilibrium with Q if melt (opening) rate equals creep (closure) rate, in which case Röthlisberger (1972) predicts

$$R \propto Q^{9/22} \tag{12}$$

160 $$S \propto Q^{-2/11}. \tag{13}$$

For a steady-state channel not at equilibrium with Q and that responds solely through changes in pressure gradient S (i.e. R is constant) Röthlisberger (1972)' equations show that:

$$S \propto Q^2. \tag{14}$$

Further details on the derivation of these equations from Röthlisberger (1972) can be found in Supplementary Sect. S2. Later
165 we compare our inversions of changes in R and S (using seismic observations) with changes in R and S as predicted by the theory of Röthlisberger (1972) for steady-state channels at equilibrium or not at equilibrium with water discharge.

3 Field setup

3.1 Site and glaciological context

Glacier d'Argentière is a temperate glacier located in the Mont Blanc mountain range (French Alps, see Fig. 2). The glacier is
170 c. 10 km long and covers an area of c. 12.8 km^2. It extends from an altitude of c. 1700 m above sea level (asl) up to c. 3600 m asl in the accumulation zone. Its cumulative mass balance has been continuously decreasing from -6 m water equivalent (w.e) in 1975 to -34 m w.e presently compared to in the beginning of the twentieth century (Vincent et al., 2009). This site is ideal to study subglacial channels properties since it presents a typical U-shaped narrow valley (Hantz and Lliboutry, 1983) and hard bed conditions (Vivian and Bocquet, 1973), two conditions that favor a well-developed R-channel subglacial network
175 (Röthlisberger, 1972).

In the present study we analyze the data recorded from spring 2017 to autumn 2018 with seismometers located between 2350 and 2400 m asl (Fig. 2). This location corresponds to the cross-section No. 4 monitored by the French glacier-monitoring program GLACIOCLIM (https://glacioclim.osug.fr/). There the glacier is up to c. 280 m thick (Hantz and Lliboutry, 1983,
180 updated from a radar campaign conducted in 2018). Subglacial water discharge is monitored 600 m downstream of the seismometers at 2173 m asl near the glacier ice fall in subglacial excavated tunnels maintained by the hydroelectric power company Emosson S.A. Subglacial water is almost entirely evacuated through one major snout, as supported by direct observations of very limited water flowing elsewhere. Thus discharge measured at this location is well representative of discharge subglacially routed under the seismometers location. Discharge measurements are conducted from mid-spring to early autumn with an ac-
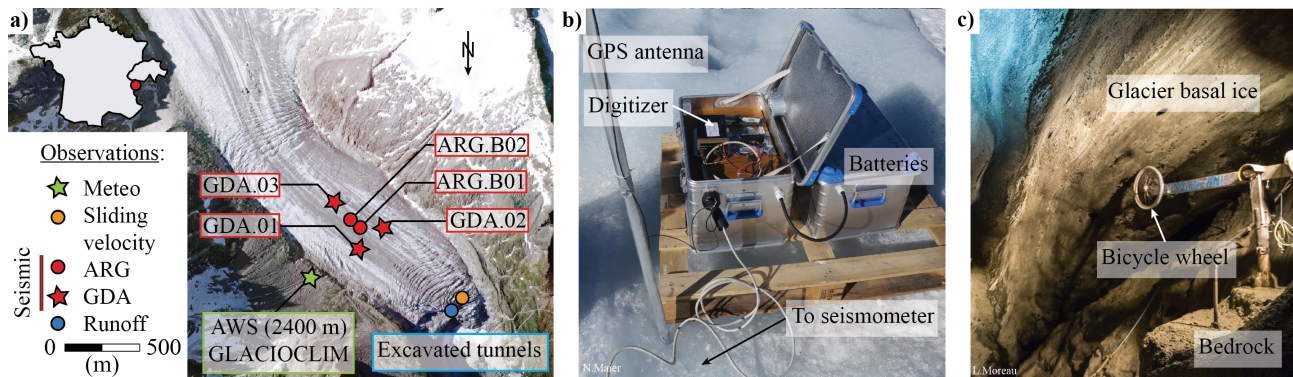
Figure 2. Monitoring setup of Glacier d'Argentière. (a) Aerial view of Glacier d'Argentière field site (France) and location of the instruments used in this study. The aerial photography was taken in 2015. The seismic network is composed of the GDA (red circles) and ARG (red stars) borehole stations and is located according to positions in summer 2018. Station ARG.B02 is installed c. 70 m deep in the ice whereas the four other stations are installed c. 5 m deep. The GLACIOCLIM (https://glacioclim.osug.fr/) automatic weather station (green star, AWS) provides air temperature and precipitation. Basal sliding speed (orange circle) and water discharge (blue circle) are measured thanks to direct access to the glacier base from excavated tunnels. Basal water pressure is measured at a similar location as that of basal sliding speed measurements. (b) Picture of the seismic instrumental setup used in this study. (c) Picture of the subglacial observatory with the bicycle wheel used to measure basal sliding speed. [Photo credits: (a) IGN France, https://www.geoportail.gouv.fr/, (b) N. Maier, (c) L. Moreau].

185 curacy of 0.01 $\mathrm{m}^3\mathrm{s}^{-1}$ every 15 min by means of a Endress Hauser sensor measuring the water level in a conduit of known geometry. The minimum measurable value for water discharge is limited by the measurement accuracy and the maximum one is of 10 $\mathrm{m}^3\mathrm{s}^{-1}$ due to the capacity of the collector. Because sediments accumulate in the collector, flushes are recorded when the latter is emptied, causing glitches in the discharge record. We remove these glitches removing Q values that present $\frac{d(Q)}{dt}$ higher than 0.2 m^3 per 15 min. Within the same tunnel network, a subglacial observatory is used to measure basal sliding

190 speed out of a bicycle wheel placed in contact with the basal ice (Vivian and Bocquet, 1973). Since August 2017 basal sliding speed is measured at a time resolution of 5 s over a 0.07 mm' space segmentation. In the close vicinity a pressure sensor, of gauged type, is used to measure subglacial water pressure with 10 min time resolution and an accuracy of 400 Pa. The sensor is installed in a borehole drilled from the excavated tunnels up to the glacier bottom (see Vivian and Zumstein (1973) for details). Air temperature and precipitation measurements are obtained at a 0.5 h time step through an automatic weather

195 station maintained by the French glacier-monitoring program GLACIOCLIM and located on the moraine next to the glacier at 2400 m asl. Precipitation is measured with an OTT Pluvio weighing rain gauge with a 400 cm^2 collecting area. When air temperature is below zero, only precipitation occurrences are accurate, but not absolute values because of snow clogging.

3.2 Seismic instrumentation

200 We use five seismic stations installed in the lower part of the glacier (Fig. 2). The instruments belong to two seismic networks, denoted as GDA (3 stations) and ARG (2 stations). Stations GDA.01, GDA.02 and GDA.03 were deployed in Spring 2017 with c. 200 m inter-station distances. These stations have digitizers of the type Nanometrics Taurus, set to 16 Vpp sensitivity and a

500 Hz sampling rate, and borehole type sensors (model Lennartz 3D/BH), with an Eigen frequency of 1 Hz. Station ARG.B01 was installed in October 2017 at the center of the GDA network at about 100 m from each GDA stations. The digitizer used for that station is a Geobit-SRi32L set to a 10 Vpp sensitivity and a 1000 Hz sampling rate. The sensor is of borehole type (model Geobit-C100) with an Eigen frequency of 0.1 Hz. Station ARG.B02 was installed in April 2018 about 50 m upglacier from station ARG.B01. The digitizer used for that station is a Geobit-SRi32 set to a 0.625 Vpp sensitivity and a 1000 Hz sampling rate. The sensor is of borehole type (model Geobit-S400), with an Eigen frequency of 1 Hz. All stations were installed c. 5 m deep below the ice surface, except ARG.B02 which was placed c. 70 m deep. A few data gaps occurred during our study due to difficulties in ensuring continuous power supply and data storage on glaciers.

4   Methodology

Refer to table C1 in Appendix C for a summary of all variables, physical quantities, and mathematical functions defined in the following sections.

4.1   Calculation of seismic power at a 'virtual' station

The raw seismic record at each station is first corrected from the sensor and digitizer responses. Then, the frequency-dependent seismic noise power P is computed using the vertical component of ground motion (see Eq.(2)). P is calculated with the Welch's method over time windows of duration dt with 50 % overlap (Welch, 1967). The longer dt, the more likely highly energetic impulsive events occur and overwhelm the background noise within that time window (Bartholomaus et al., 2015). To maximize sensitivity to the continuous, low amplitude, subglacial channel-flow-induced seismic noise and minimize that of short-lived but high energy impulsive events, we use a short time window of $dt = 2$ s to calculate P, and average it over time windows of 15 min in the decimal logarithmic space. We express P in decibel (dB, decimal logarithmic), which allows properly evaluating its variations over several orders of magnitude.

We reconstruct a two-year long timeseries by merging records from the five available stations into one unique record at a 'virtual' station. To minimize site and instrumental effects on seismic power we shift the average power at each station to a reference one taken at ARG.B01. The seismic signal at our 'virtual' station is composed of the GDA seismic signals between May 2017 end December 2017, and of the ARG seismic signals between December 2017 and December 2018 (see Fig. S1).

4.2   Evaluating bias due to anthropogenic noise

Later in section 5 we show that when water discharge Q is low (in the early and late melt season) seismic power from anthropogenic noise (P_A) is comparable to the subglacial channel-flow-induced seismic power (P_w). Here we evaluate how much P_A adding to P_w can bias the evaluation of scaling predictions of Gimbert et al. (2016). We calculate a synthetic seismic power P as $P = P_A + P_w$ and a synthetic P_w from a synthetic Q as $P_w = Q^n$ with n being equal to $\frac{5}{4}$ or $\frac{14}{3}$ as expected from theory
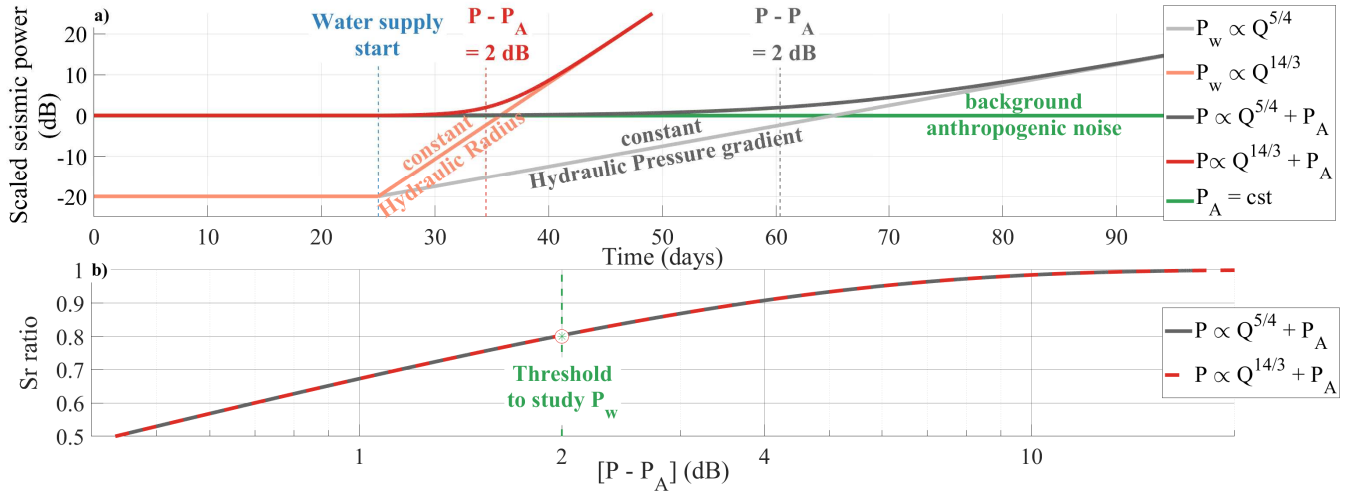
Figure 3. Synthetic predictions of scaling bias due to anthropogenic noise superimposing to subglacial channel-flow-induced seismic noise. (a) Synthetic anthropogenic seismic power (green line, P_A), synthetic subglacial channel-flow-induced seismic power $P_w = Q^n$ with Q the synthetic water discharge for $n = \frac{5}{4}$ (grey line) and $n = \frac{14}{3}$ (orange line) and synthetic seismic power $P = P_A + P_w$ for $n = \frac{5}{4}$ (black line) and $n = \frac{14}{3}$ (red line). (b) Evolution of Sr (see Sect. 4.2) ratio with respect to P-P_A for $n = \frac{5}{4}$ (grey line) and $n = \frac{14}{3}$ (red line). Note that the two curves overlap.

(see Eqs.(8) and (9)). We quantify the relative contributions of P_w and P_A to P through the parameter Sr, which we define as

235 $Sr = log\left[\left(\frac{Q}{P}\right)^n\right]$. When Sr tends to 1, subglacial channel-flow-induced seismic power dominates the synthetic seismic power and when Sr tends to 0 anthropogenic noise power does.

In Fig. 3(a) we show the temporal evolution of synthetic P with a constant value for P_A and with a P_w that responds to a synthetic evolving water supply Q. The value of P is normalized by P_A, resulting in $P = 0$ dB in winter. For $P_w \propto Q^{14/3}$

240 (Fig. 3(a), red and orange lines), P_w dominates the contribution to P within c. 10 days from the onset of water supply. For $P_w \propto Q^{5/4}$ (Fig. 3(a), black and green lines) P contains both P_w and P_A contributions during a period that is three times longer than for $P_w \propto Q^{14/3}$. The evolution of Sr with respect to P-P_A (Fig. 3(b)) is the same for both the constant hydraulic pressure gradient (red line) and constant hydraulic radius (grey line) scenarii. For P-$P_A > 2$ dB, Sr is higher than 0.8, meaning that subglacial channel-flow-induced seismic power contributes by more than 80% to the synthetic seismic power. Later in

245 Sect. 5.2 we measure P_A during winter and use the condition P-$P_A > 2$ dB to define the periods where evaluate P_w directly from the measurement of P and investigate the subglacial hydraulic properties.

4.3 Definition of metrics to evaluate sub-diurnal dynamics

Since the P_w versus Q relationship is not unique and may vary with time (see Sect. 2), we expect that the diurnal timeseries of P_w versus Q may exhibit different patterns throughout the melt season; and that these patterns reveal changes in the subglacial

250 hydraulic properties. To systematically quantify the diurnal variability of P_w, Q, R and S throughout the melt season we define

three metrics that we calculate on an hydrological daily basis (defined as the period between two minimum Q within a 24 h time window). To focus on the diurnal variability only, we bandpass filter our timeseries within a [6-36] h range (see Appendix Fig. A1 for details). Our first metric quantifies the diurnal variability of a given variable X during a given day and corresponds to the coefficient of variation C_v defined as:

$$C_v = \frac{(X_{day})_{max} - (X_{day})_{min}}{\overline{X_{day}}} \qquad (15)$$

with $(X_{day})_{max}$ and $(X_{day})_{min}$ the maximum and minimum value of X_{day}, respectively, and $\overline{X_{day}}$ its average. Our second metric ϕ quantifies daily hysteresis between P_w and Q by evaluating the difference between P_w when Q is rising, e.g. in the morning, and P_w when Q is falling, e.g. in the afternoon. Following the approach of Roth et al. (2016) we define ϕ as:

$$\phi = \frac{\overline{(P_{w,day})_{rising}} - \overline{(P_{w,day})_{falling}}}{\overline{(P_{w,day})_{falling}}}. \qquad (16)$$

The larger ϕ, the more seismic energy is recorded during the rising discharge period with respect to the falling one. Hysteresis can occur either because of an asymmetry between $(P_{w,day})_{rising}$ and $(P_{w,day})_{falling}$ or because of a time lag between P_w and Q. To avoid ambiguity between these two hysteresis sources our third metric corresponds to the daily time lag δt between the time $t((P_{w,day})_{max})$ when P_w is maximum and the time $t((Q_{day})_{max})$ when Q is maximum and is defined as:

$$\delta t = t((Q_{day})_{max}) - t((P_{w,day})_{max}). \qquad (17)$$

We set the condition that for δt to be calculated, $t((P_{w,day})_{max})$ has to correspond to both the time when P_w is maximum and has a null-derivative within a [-8, 8] h' time window around $t((Q_{day})_{max})$. We note that a time delay of about 0.04 h is expected due to water flowing at c. 1 m.s^{-1} over the c. 600 m separating our seismic stations to where Q is measured (see Fig. S2 for details). This means that any values of δt greater than $\pm$ 0.04 h are not attributable only to water transfer time lags.

5 Results

5.1 Overview of observations

Seismic power P as calculated at our 'virtual' station based on records from our 5 stations (see Sect. 4) is shown in Fig. 4(a) as a function of time (May 2017 to December 2018) and frequency (2 to 100 Hz). Large seasonal changes in P are observed within the [2-10] Hz frequency range, in which P is higher by more than 2 orders of magnitude during the melt season (mid-May to September) compared to in winter. Changes in P are also observed within the [10-20] Hz frequency range with P during the melt season being about an order of magnitude larger than in winter. Significant changes of smaller amplitude are also observed at higher frequency ([20-100] Hz). Spectral distributions of P presented in Figs. 4(b) and (c) show widely spread P-values during the melt season (Fig. 4(b), variations over more than 10 dB), as opposed to being comparatively much nar-
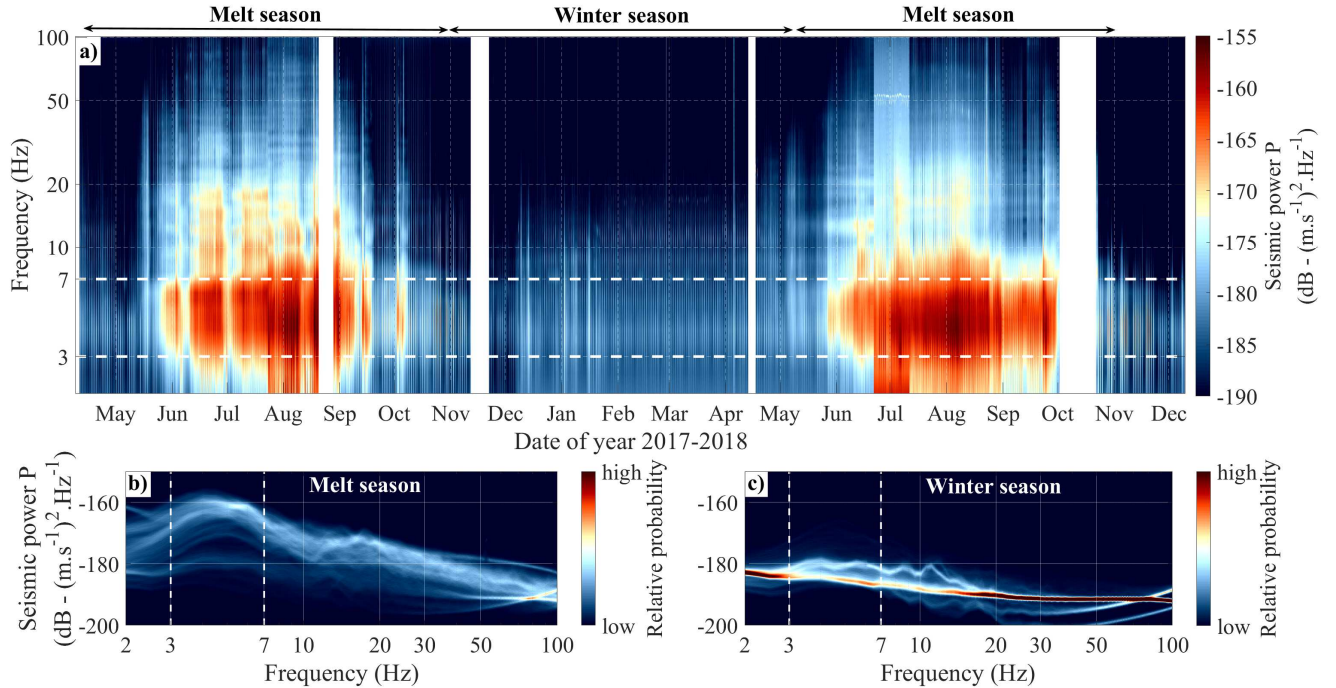
Figure 4. (a) Spectrogram of the observed seismic power P as a function of time (x-axis, May 2017 to December 2018) and frequency (y-axis, 1-100 Hz log-scale). Colors represent seismic power in decimal logarithmic (dB) relative to $(\text{m.s}^{-1})^2.\text{Hz}^{-1}$. White bands correspond to data gaps. (b) and (c) Spectral distribution of seismic power during the melt seasons (b) and the winter seasons (c). Colors represent occurrence probability and colorbars are identical for (b) and (c).

rower in winter (Fig. 4(c), variations within 1-3 dB). Seismic power within the [3-7] Hz frequency range shows the highest range of variations from winter to summer (Figs. 4(a) and (b)). Over the two years, the overall spectral pattern remains simi-

280   lar, although intra-seasonal variations of P during the 2017 melt season are more pronounced compared to the 2018 melt season.

      The observed meteorological and hydrological conditions at Glacier d'Argentière together with the measured basal sliding speed and the seismic power $P_{[3-7]\,\text{Hz}}$ as averaged within the [3-7] Hz frequency range are shown as a function of time (May 2017 to December 2018) in Fig. 5. Water discharge Q shows a strong seasonal signal with discharge lower than $0.1\ \text{m}^3.\text{s}^{-1}$

285   in winter and up to values higher than $10\ \text{m}^3.\text{s}^{-1}$ in summer. These changes are consistent with air temperature values, and occur concomitantly with the evolution of $P_{[3-7]\,\text{Hz}}$ (Fig. 5(b)). Further details on the comparison between $P_{[3-7]\,\text{Hz}}$ and Q are presented in Sect. 5.2. Over the first months of the melt season (early May to mid-June 2017 and late April to mid-June 2018) Q increases by about 2 orders of magnitude from 0.1 to $10\ \text{m}^3.\text{s}^{-1}$. At the same time, the amplitude of the diurnal variations in Q increases up to $3\ \text{m}^3.\text{s}^{-1}$ over the summer. The evolution of basal sliding speed presented in Fig. 5(c) depicts a rapid

290   acceleration from $5\ \text{mm.h}^{-1}$ in May 2017 and April 2018 to $7\ \text{mm.h}^{-1}$ over the following month. Sliding speed then stays almost constant through the summer, and slowly decreases down to a minimum of $4.5\ \text{mm.h}^{-1}$ in February (see also comparable
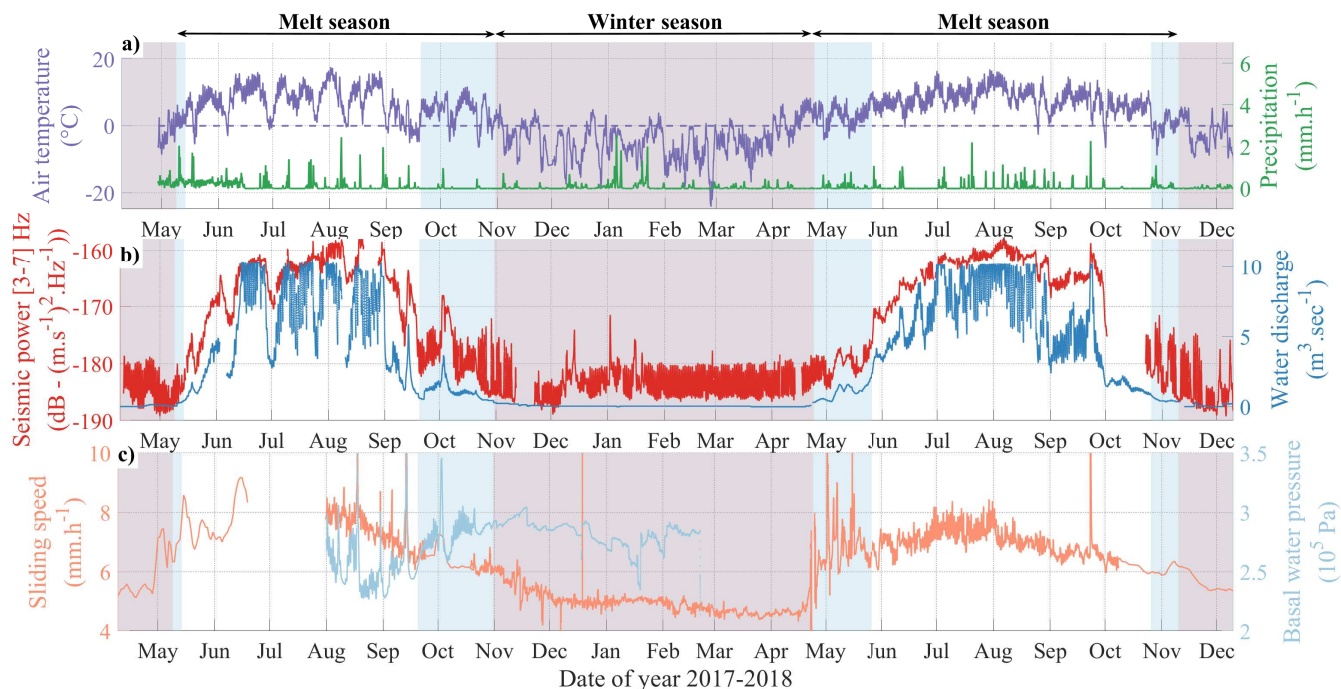
Figure 5. Timeseries of physical quantities measured from spring 2017 to winter 2018 at Glacier d'Argentière. All data are smoothed over a 6 h time-window. (a) Surface air temperature (purple line) and precipitation (green line) at the GLACIOCLIM AWS (Fig. 2). The dashed purple line shows $T = 0°C$. (b) Averaged seismic power within the [3-7] Hz frequency range at the 'virtual' seismic station (red line, $P_{[3-7]\,\mathrm{Hz}}$, see Sect. 5.2 for details) and subglacial water discharge Q (blue line). (c) Basal sliding speed (orange line) and subglacial water pressure (light blue line) measured at Glacier d'Argentière subglacial observatory (Fig. 2). Note that temporal resolution in the sliding speed is lower in [May-July] 2017 and from October 2018 because of instrumental issues. Red shaded areas represent the winter season; blue shaded areas represent the periods when diurnal changes in anthropogenic noise are too pronounced to study P_w on a diurnal basis.

observations made by Vincent and Moreau (2016) over the past decade). Basal water pressure measurements (Fig. 5(c)) show that at the seasonal timescale the basal water pressure tends to be higher in winter than in summer by c. 2.5 1e^{+4} Pa. In summer 2017 the short-term (diurnal) variability in the basal water pressure is more pronounced than in winter, as also observed for the water discharge (Fig. 5(b) and Fig. A1). During heavy rainfall (Fig. 5(a)) and consequent discharge (Fig. 5(b)), basal water pressure variations are in phase with sliding speed (Fig. 5(c); e.g in August 1st, August 7th, August 18th, August 30th, September 13th or October 2nd of 2017). This evolution of the measured basal water pressure rather depicts a local behavior whereas changes in the basal sliding speed (Fig. 5(c)) rather represent average changes in the average basal water pressure conditions over our study area and therefore better represent the global cavity-system pressure conditions.

Measurement artifacts are observed for Q with values being thresholded at $10\,\mathrm{m^3.s^{-1}}$, and for P in July 2018 when unusually high seismic power values are observed over the whole frequency range, which we associate with the initially weak ice-sensor coupling of ARG.B02. Site specificity of the GDA network used in 2017 causes higher seismic power in the [8-20] Hz

frequency band in 2017 than in year 2018. These artifacts appear to not significantly affect P (at least not within the [2-10] Hz
frequency range), nor the concomitant temporal evolution of P and Q over the two years.

5.2   Seismic power induced by subglacial channel-flow

We consider seismic power $P_{[3-7]\,\text{Hz}}$ averaged within the [3-7] Hz frequency range (Fig. 5(b) (red line)) as best representative
of subglacial channel-flow-induced seismic power P_w because it shows the highest variations with changes in Q (Figs. 4 and 5).
A similar frequency-signature of the subglacial channel-flow-induced seismic noise as been observed by Bartholomaus et al.
(2015), Preiswerk and Walter (2018) and Lindner et al. (2019). This frequency range is also comparable to those observed for
water flow in rivers (Schmandt et al., 2013; Gimbert et al., 2014). As Q increases from less than $0.1\ \text{m}^3.\text{s}^{-1}$ in early May to
about $10\ \text{m}^3.\text{s}^{-1}$ end of July, P_w increases by up to 30 dB (i.e. 3 orders of magnitude). Differences in relative variations of
P_w across stations are lower than 0.5 dB including during periods of high discharge (Fig. S2). This supports the accuracy and
validity of our 'virtual' station reconstruction to study the subglacial channel-flow-induced seismic power (Sect. 4). Variations
in P_w follow those of Q during the melt season and over seasonal to weekly times scales (Fig. 5(b)). Both the high sub-monthly
variability in Q and air temperature observed in 2017 and the rapid changes in Q occurring in fall 2017 and 2018 are also
observed in the temporal evolution of P_w. In winter we observe high seismic power bursts from December to mid-January
occurring when Q is null but concomitantly with the beginning of heavy snowfall events. These bursts are not associated with
subglacial channel-flow-induced seismic noise but likely correspond to repeating stick-slip events triggered by snow loading
similar to those observed previously by Allstadt and Malone (2014). When Q is lower than $2\ \text{m}^3.\text{s}^{-1}$ during winter, early spring
and fall, we observe regular weekly and daily variations in $P_{[3-7]\,\text{Hz}}$ that superimpose to the background variations (Fig. 5(b)).
This regular pattern corresponds to anthropogenic noise, as previously observed by Preiswerk and Walter (2018) in a similar
setup.

Based on the condition proposed in Sect. 4.2 (P-$P_A > 2$ dB) we use the periods [May 14th - November 1st] 2017 and
[April 21th - November 10th] 2018 to investigate the subglacial hydraulic properties (white and blue areas in Figs. 5 and 8).
During these periods we subtract the mean winter diurnal pattern of P_A (defined between January 29th and April 4th 2018)
from $P_{[3-7]\,\text{Hz}}$ to obtain P_w (Fig. S3). At the diurnal scale, because P_A can slightly vary from day to day depending on the
anthropic activity (e.g higher anthropic activity during working days than holidays), the periods of very early and very late
melt season are still strongly influenced by day-to-day changes in P_A. To study diurnal changes in P_w without being biased by
anthropogenic noise we limit our analysis to the periods [May 15th - September 22st] 2017 and [May 27th - October 28th]
2018 (white areas in Figs. 5 and 8; based on direct observation shown in Fig. S3). Later in Sect. 5.4 we filter P_w with a 5-day
lowpass filter (i.e. removing variability lower than 5 days) when inverting for the hydraulic properties. Doing so allows to study
with confidence the early and late melt-season by reducing the influence of the diurnal variability in P_A on P_w while keeping
sub-weekly variations in P_w and Q (see Fig. S4 for details).
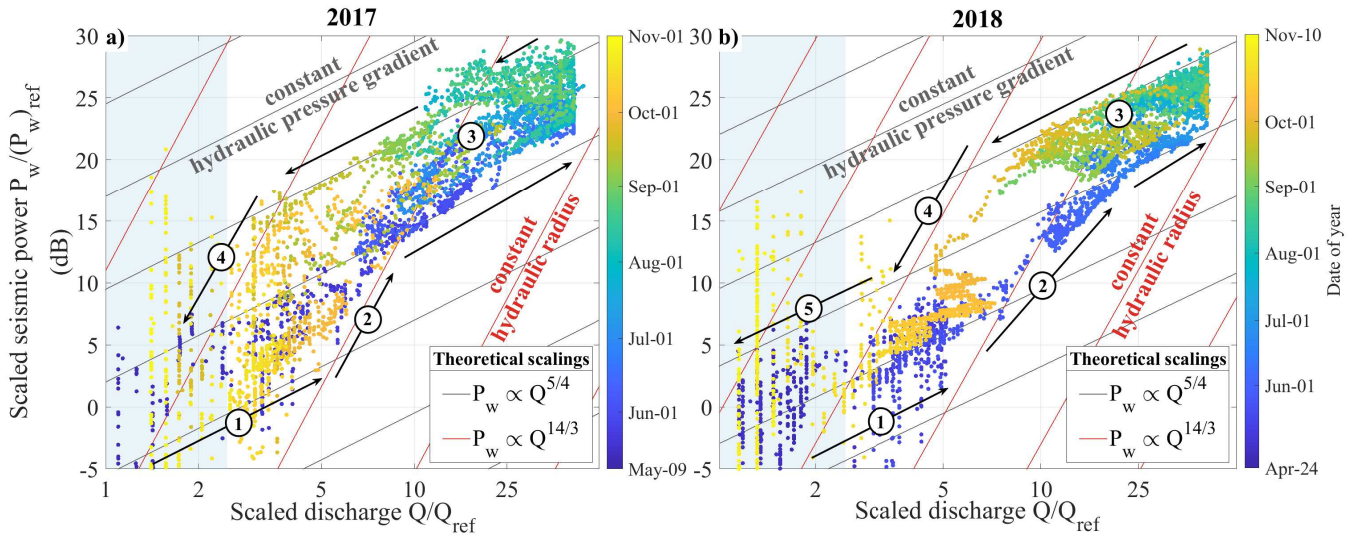
Figure 6. Observed (dots) and predicted (lines) changes in subglacial channel-flow-induced seismic power $\frac{P_w}{(P_w)_{ref}}$ versus changes in water discharge $\frac{Q}{Q_{ref}}$ during the melt season of years 2017 (a) and 2018 (b). Temporal signals are filtered with a 1-h lowpass filter. The color scale differs for the two years and varies with time from early April to mid-November. Lines show predictions calculated from Eqs.(8) and (9) for constant hydraulic radii and varying hydraulic pressure gradient (red lines) and for constant hydraulic pressure gradient and varying hydraulic radii (black lines). Blue shaded areas represent the period when Q is lower than 1 $m^3.s^{-1}$. Arrows show the direction of time and circled numbers refer to periods described in the main text. Reference values $(P_w)_{ref}$ and Q_{ref} are taken the first day of the 2017 melt-season (May 10th 2018).

5.3 Comparison of observations with predictions from Gimbert et al. (2016)

5.3.1 Analysis of seasonal changes

Seasonal scale observations and predictions of the subglacial channel-flow-induced seismic power P_w versus water discharge
340   Q are shown in Fig. 6. We find that theoretical predictions from Gimbert et al. (2016) (red and black lines) are consistent with our observations (colored dots), which exhibit a general trend between that predicted at constant hydraulic pressure gradient (Fig. 6, see black lines calculated using Eq.(7)) and that predicted at constant hydraulic radius (Fig. 6, red lines calculated using Eq.(6)). As Q increases at the very onset of the melt season (in end of April), observed P_w-values follow the trend predicted under constant hydraulic pressure gradient (Fig. 6 ①). As Q increases more rapidly from mid-May to end of June (Fig. 5(b)),
345   P_w follows a different trend of evolving hydraulic pressure gradient (Fig. 6 ②). The general trend from July to September is then dominated by changes in hydraulic radius (Fig. 6 ③). As Q decreases during the melt season termination, observed P_w values follow the trend of evolving hydraulic pressure gradient in a similar manner as during the early melt season (Fig. 6 ④). At the end of the melt season 2018 (Late October to November) our observations also show a trend of changing hydraulic radius although this observation is not as clear in 2017 (Fig. 6 ⑤). A clear counter-clockwise seasonal hysteresis of up to 10
350   dB power difference is observed in Fig. 6 between P_w and Q. This shows that for a similar water discharge, higher subglacial channel-flow-induced seismic power is generated in the late melt season compared to in the earlier melt season. The 10 m^3s^{-1}
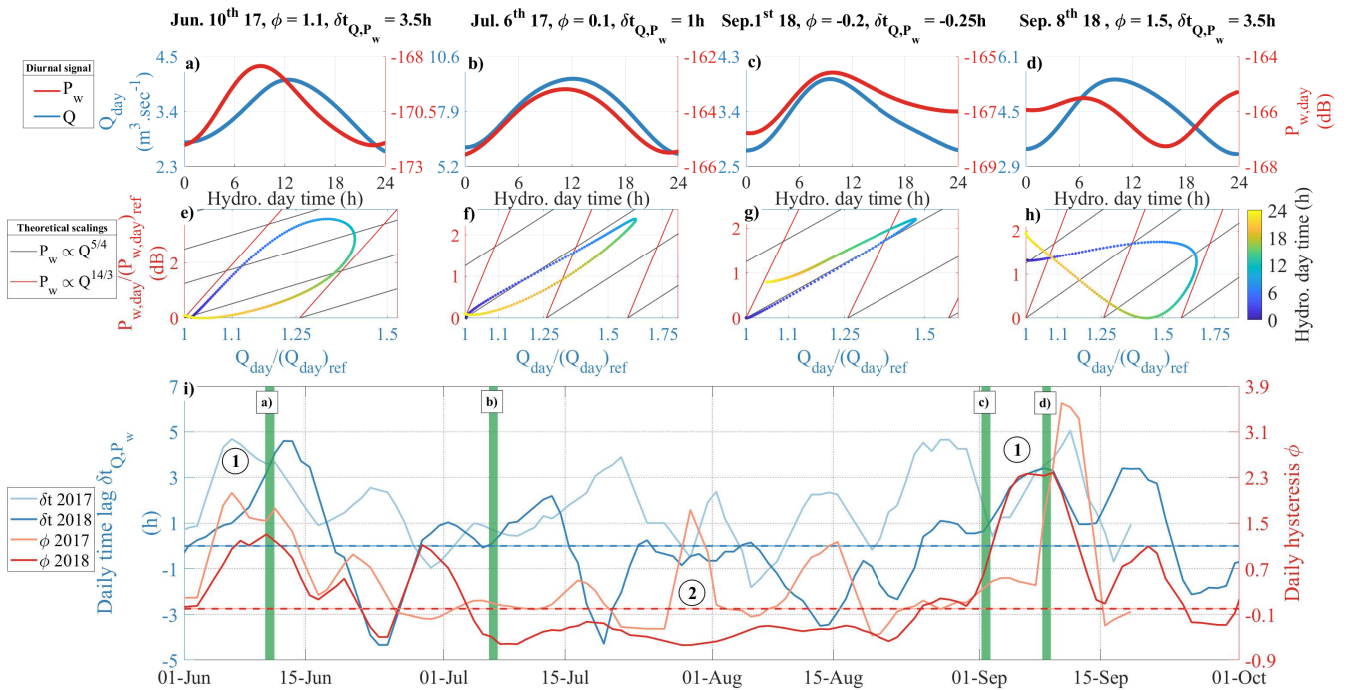
Figure 7. Diurnal observations of the subglacial channel-flow-induced seismic power P_w and water discharge Q and comparison with predictions from Gimbert et al. (2016). (a) to (d) Daily evolution of the [6-36] h bandpass filtered seismic power $P_{w,day}$(red line) and water discharge Q_{day} (blue line) for four selected hydrological days. Values of $P_{w,day}$ and Q_{day} are centered on the average respective absolute value of the corresponding day. Corresponding values of daily $\delta t_{Q,P_w}$ and ϕ are shown top of the panels. (e) to (h) Observed (colored dots) and predicted (red and black lines calculated with Eqs.(6) and (7)) P_w versus Q daily relationships. Note that y-axis bounds differs from panel to panel. Both variables are normalized by their daily minima. (i) Daily time lag $\delta t_{Q,P_w}$ between $P_{w,day}$ and Q_{day} peaks (blue lines) and daily hysteresis ϕ between $P_{w,day}$ and Q_{day} (red lines). Shaded lines are data of year 2017, plain ones of year 2018. Dashed lines show $\delta t_{Q,P_w} = 0$ (blue) and $\phi = 0$ (red). Timeseries are smoothed over 5 days. Green vertical bars show times of the four selected hydrological days with the corresponding panel number. Circled numbers refer to the two phases described in the main text.

measurement threshold in Q is well observable for the two years but does not bias the observed scaling of changing hydraulic radius observed during summer.

5.3.2 Analysis of diurnal changes

355 Observations and predictions of the diurnal relationship between the subglacial channel-flow-induced seismic power P_w and water discharge Q throughout the melt season are shown in Fig. 7. We quantify the diurnal behaviors over the two melt seasons by calculating the hysteresis amplitude ϕ and time lag δt (see Sect. 4.3) and through comparing our observations with the theoretical predictions calculated for four selected days (panels (a) to (h) in Fig. 7). We selected these days based on three criteria: they represent typical variations of P_w and Q over their respective periods ($\sim \pm 5$ days around their date); they show that our

360 observations capture diurnal variations from unique days without multi-days averaging; they give a pedagogical support for the reader to interpret values of the hysteresis amplitude ϕ and time lag δt shown in Fig. 7i. We focus on these two indicators as

they allow to evaluate respective changes of P_w versus Q.

The seasonal evolution of the daily hysteresis amplitude ϕ presents two peaks in late-May / early-June and in late-August / early-September, which are consistently observed in both 2017 and 2018 (phases ① in Fig. 7(i)). The seasonal evolution of the diurnal time lag between δt of P_w to Q is similar to that of ϕ, with peak values at $\delta t > 2.5$ h in late-May / early-June and in late-August / early-September (Fig. 7(i)). This supports that hysteresis is mainly caused by phase difference between P_w and Q rather than by asymmetrical changes P_w when Q rises compared to when Q falls Q (Sect. 4.3). The variability of δt over the season is much larger than the predicted 0.04 h instrumental time lag (see Sect. 4.3), such that its evolution represents real changes in the relationship between P_w and Q.

In the early and late melt season (phases ① in Fig. 7(i)), $P_{w,day}$ peaks, in average, more than 3 h before Q_{day} (e.g. Fig. 7(e)). These long time delay δt are concomitant to a pronounced asymmetrical shape in $P_{w,day}$ with a steeper rising than falling limb (e.g. Fig. 7(e)). This results to large clockwise hysteresis in $P_{w,day}$ versus Q_{day} as well pictured by the high hysteresis values during these periods ($\phi > 1$, phases ① in Fig. 7(i)). For example, on June 10th our observations follow the trend of evolving hydraulic pressure gradient in the morning and the one of changing hydraulic radius in the afternoon and at night. On September 8th our observations follow the trend of changing hydraulic radius in the early morning and the one of evolving hydraulic pressure gradient in the afternoon. On the contrary to these periods, in summer (phase ② in Fig. 7(i)), both ϕ and δt are low with $\phi \simeq 0$ and 2 h $> \delta t >$ -2 h. At this time, δt has a more pronounced seasonal and year-to-year variability than ϕ (Fig. 7(i)) with values oscillating within [2 ; -2] h and minimum values reaching $\delta t <$ -4 h. In July and August (e.g. panels (b) and (c) in Fig. 7), P_w peaks nearly at the same time as Q with $\delta t < 0.5$ h and with an almost symmetrical diurnal evolution (Fig. 7(i)). For both summer days (July 6th and September 1st), our observations mainly follow the trend of changing hydraulic radius throughout the whole day, with a non-null hysteresis that shows that hydraulic pressure gradient may also change. This two-phases seasonal evolution shows that the early and late melt season diurnal changes in Q cause a pronounced diurnal variability in the hydraulic pressure gradient and limited diurnal changes in the hydraulic radius, whereas over the summer channels show a more marked response to diurnal changes in Q through changes in hydraulic radius.

5.4   Inversions of changes in hydraulic radius and hydraulic pressure gradient

We invert for the relative changes of hydraulic radius $\frac{R}{R_{ref}}$ and hydraulic pressure gradient $\frac{S}{S_{ref}}$ using Eqs.(10) and (11) and our observations of timeseries of Q and P_w once filtered with a 5-day lowpass filter (see Fig. S4 and Sect. 5.2 for details). In the following for the sake of readability we use the notation R, S and V to refer to $\frac{R}{R_{ref}}$, $\frac{S}{S_{ref}}$ and the relative basal sliding speed $\frac{V}{V_{ref}}$. Reference values for these three variables are taken as their minimum value over the two years, which occur on May 10th 2017 for R, May 14th 2018 for S and March 28th 2018 for V.
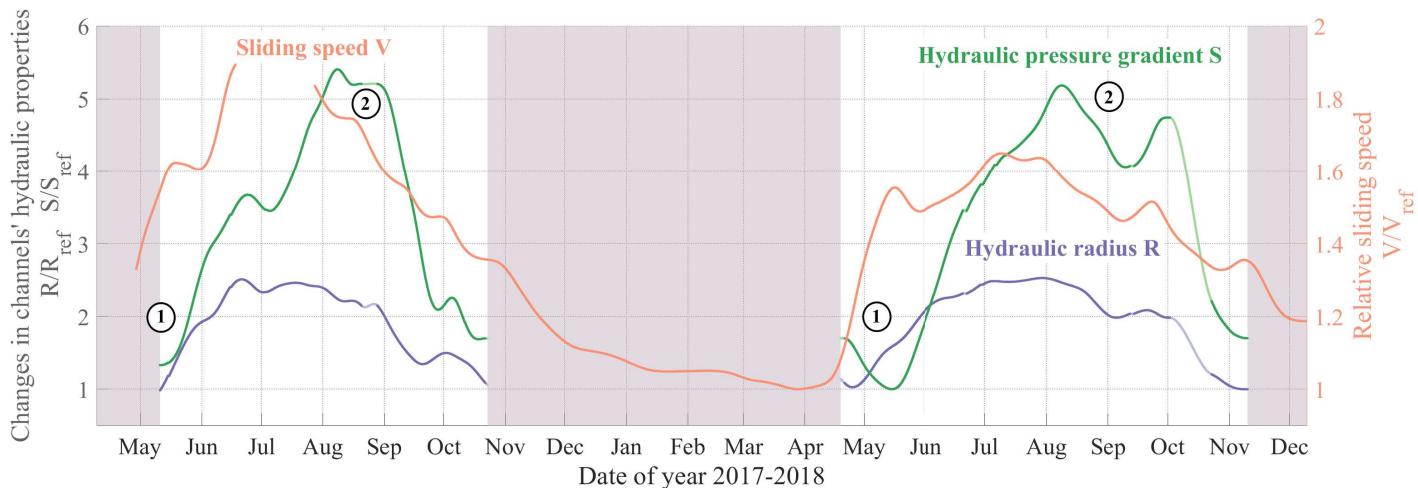
Figure 8. Seasonal evolution of the hydraulic radius and hydraulic pressure gradient as inferred from seismic observations as well as of glacier basal sliding speed as measured in-situ. (a) Relative hydraulic pressure gradient $\frac{S}{S_{ref}}$ (green line), relative hydraulic radius $\frac{R}{R_{ref}}$ (purple line) and relative sliding speed (orange line). Red shaded areas represent the winter season. Temporal signals of R and S are calculated using 5-day lowpass filtered timeseries of Q and P_w and are further smoothed applying a 30-day lowpass filter. Shaded lines correspond with period with no data and show interpolated values of R and S using a cubic spline interpolation. Reference values for the three variables are taken as their minimum value of the two years (i.e. May 10th 2017 for R, May 14th 2018 for S and March 28th 2018 for V). Circled numbers refer to the three phases described in the main text.

5.4.1 Analysis of seasonal changes

The temporal evolution of R, S and V are presented in Fig. 8. We recall here that the changes in V can be considered as a
395   good proxy for changes in water pressure in the subglacial cavity network (see Sect. 5.1 for details). We find that all three variables show a well-marked seasonal evolution, with low values during the early and late melt season and high values in summer. However, differences between R, S and V exist over the melt season. For both years, R starts increasing from the onset of the early melt season, until reaching a maximum within two months in late-June to early-July. R is then two times larger in average than in the early melt season. In contrast, during the first weeks of the melt season 2018, S rapidly decreases (Fig. 8
400   ①), concomitantly with an abrupt increase in V by a factor of 1.5 compared to winter. This shows that as the average water pressure rises in cavities and enhance sliding, channels on the contrary undergo depressurization. During the melt season 2017 we do not observe such behavior possibly because of a timeserie of P_w that starts about three weeks later than in 2018. The increase in S then occurs with a delay of about one month in 2018 and of about one week in 2017 compared to that in R, and S reaches a maximum in August (Fig. 8 ②). S is at that time on average five to six times larger than in the beginning of the
405   melt season. As S increases, V and R have already past their summer maximum. Contrary to the conclusions obtained on the Mendenhall Glacier (Alaska) where S presents no significant trend over the two-month long investigated period (Gimbert et al., 2016), seasonal changes in water discharge at Glacier d'Argentière are inferred to cause changes in both R and S. From early to mid-September, R and S decrease concomitantly and reach their minimum in late October. The summer to winter transition
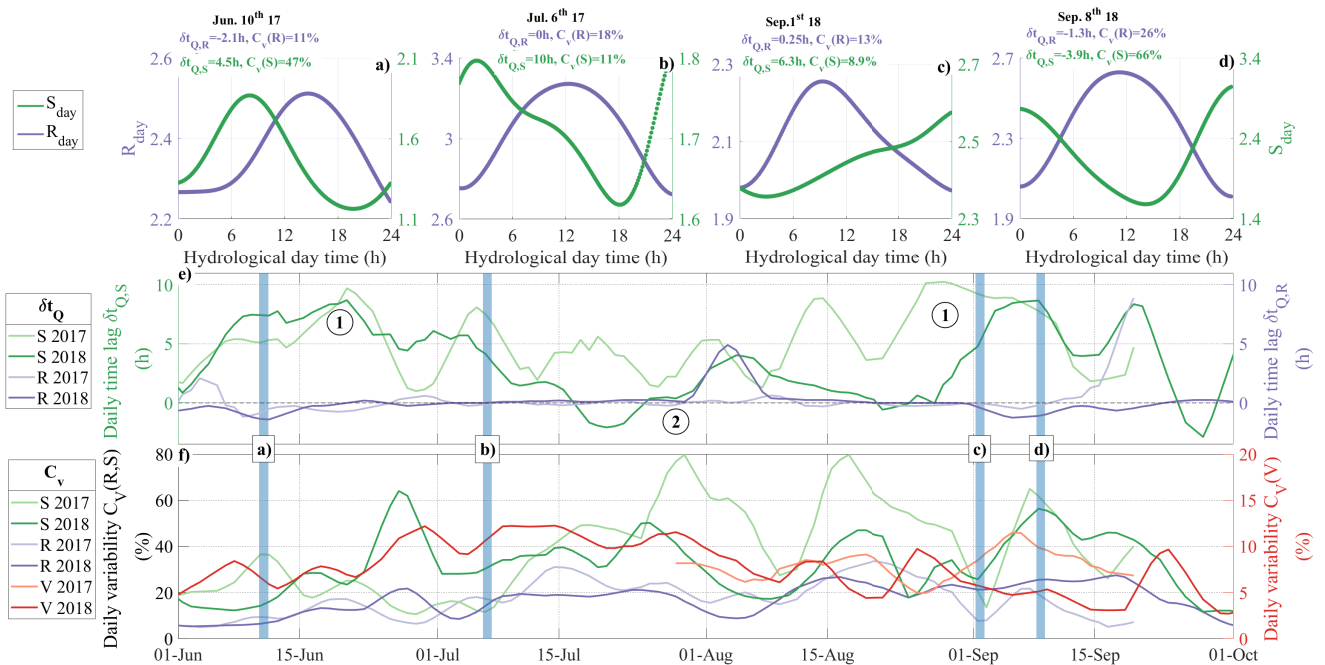
Figure 9. Diurnal evolution of the hydraulic radius R and hydraulic pressure gradient S and comparison to glacier dynamics. (a) to (d) Daily timeseries of R (purple line) and S (green line) for four selected hydrological days across the melt season. Timeseries are band-pass filtered within [6-36] h. Values of R_{day} and S_{day} are centered on the average respective absolute value of the corresponding day. Corresponding daily values of $\delta t_{Q,R}$, $\delta t_{Q,S}$, $C_v(R)$ and $C_v(S)$ are shown top of the panels. Note that y-axis bounds differ from panel to panel. (e) Daily time lags $\delta t_{Q,R}$ between R_{day} and Q_{day} peaks (purple lines) and $\delta t_{Q,S}$ between S_{day} and Q_{day} peaks (green lines). (f) Sub-diurnal variability C_v of R (purple lines), S (green lines) and the basal sliding speed V (red line). Timeseries are smoothed over 5 days. Blue vertical bars shows location of the four selected days with the corresponding panel. Shaded lines are data of year 2017, plain lines are data of year 2018. Circled numbers refer to the two phases described in the main text.

is most pronounced for S, which decreases by about a factor of 4 within less than a month (September to October) while R
410 decreases more gently.

5.4.2 Analysis of diurnal changes

Figure 9 describes how channel and cavity properties behave at the diurnal scale throughout the melt season. We quantify the diurnal behavior throughout the two melt seasons with the time lag δt between R and Q daily maxima, noted $\delta t_{Q,R}$, and
415 between S and Q daily maxima, noted $\delta t_{Q,S}$. We also calculate the amplitude of the diurnal variations C_v for R, S and V (see Sect. 4.3 for definitions). In the same scopes as in Sect. 5.3.2 we illustrate in panels (a) to (d) in Fig. 9 the diurnal evolution of R and S for the same four selected days as in Fig. 7.

$C_v(R)$ and $C_v(S)$ both present seasonal variation, with maximum values being reached mid-summer. The amplitude of $C_v(S)$ is however up to three-times larger than that of $C_v(R)$ since $C_v(S)$ reaches up to 80 % in August while $C_v(R)$ only increases up to 30 % for (Fig. 9(f)). In contrast, the seasonal evolution of $\delta t_{Q,R}$ and $\delta t_{Q,S}$ drastically differs (Fig. 9(e)). On one hand, the temporal evolution of $\delta t_{Q,R}$ presents no marked changes throughout the season and generally remains within a range of $\pm$ 1 h (Fig. 9(e)) as highlighted by the four selected days (Figs. 9(a) to (c)). This shows that R and Q are consistently in phase on a diurnal basis throughout the melt season. On the other hand, the temporal evolution of $\delta t_{Q,S}$ presents average values of about 5 h with two peaks of $\delta t_{Q,S} > 8$ h in June and August (Fig. 9(e) ①) and a period of low values ranging within [0;5] h in mid-summer (Fig. 9(e) ②). These changes in S are clearly observed in the diurnal snapshots (e.g. Figs. 9(a) to (d)) that show a marked increase in hydraulic pressure gradient in the morning before the rise in hydraulic radius. Such a difference in diurnal dynamics between R and S shows that channels exhibit high hydraulic pressure gradients in the early morning time while their hydraulic radius grows slowly to reach its maximum at the same time as the water discharge does.

We also compare in Fig. 9(f) the diurnal dynamics of channel properties to the diurnal dynamics of the average water pressure conditions in cavities by comparing $C_v(R)$ and $C_v(S)$ with $C_v(V)$. Over the melt season, $C_v(V)$ exhibits a pattern that is similar to $C_v(R)$ and $C_v(S)$, with higher values observed for the three variables in summer (> 10 %) than during the early and late melt season (< 10 %). This shows that short-term variability in channels properties (i.e. R and S) correlates well with the short-term variability in average water pressure condition in cavities. From late August to mid-September 2017, we observe that $C_v(S)$ reaches up to 60 % over less than a week, followed c. a week later by a rapid rise in $C_v(V)$ (Fig. 9(f)).

5.5 Comparison of inversions with predictions from Röthlisberger (1972)

Our seismically derived S and R values are shown in Fig. 10 as a function of relative changes in water discharge Q, along with scaling predictions calculated using the theory of Röthlisberger (1972) assuming channels at equilibrium (melt rate equals creep rate) with $S \propto Q^{-2/11}$ and $R \propto Q^{9/22}$ (Eqs.(14) and (12), green lines in Fig. 10) and channels out-of-equilibrium that respond to changes in Q only through changes in S with $S \propto Q^2$ and R is constant (Eq.(13), purple lines in Fig. 10). We find that R and S generally exhibit variations with Q that lie between those expected for channels at equilibrium and those expected for channels evolving at constant hydraulic radius. At low discharge ($\frac{Q}{Q_{ref}} < 4$, $Q < 1$ m^3.s^{-1}) during the early and late melt season (Fig. 10 ①) our derived changes in S and R with Q approach the theoretical prediction for channels behaving at equilibrium. At high discharge ($\frac{Q}{Q_{ref}} > 4$, $Q > 1$ m^3.s^{-1}; mid-May to early October, Fig. 10 ②) changes in S and R with changes in Q significantly departs from predictions of channels at equilibrium and approaches the one of channels evolving out-of-equilibrium through changes in S solely. The transition between the two regimes herein observed is quite abrupt for S which switches from being a decreasing to being an increasing function of Q. For R, the transition is marked by a weaker dependency on Q as thi latter is high. During the period when $Q/Q_{ref} > 5$, best datafit of R with Q gives $R \propto Q^{0.27} \propto Q^{6/22}$ and for the periods when $Q/Q_{ref} < 4$ it gives $R \propto Q^{0.36} \propto Q^{8/22}$. This latter scaling is similar to the predicted scaling of $R \propto Q^{9/22}$ calculated using the theory of Röthlisberger (1972) assuming channels at equilibrium.
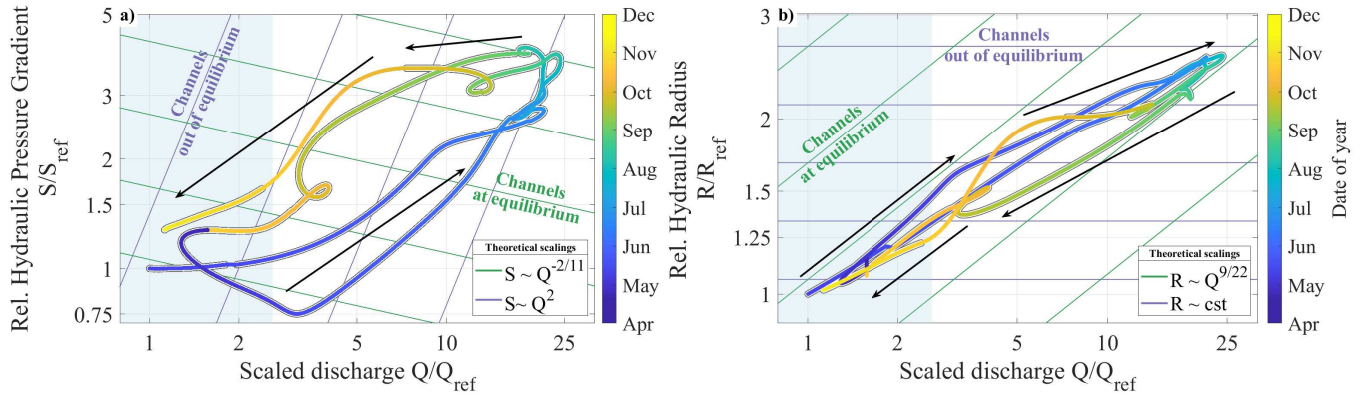
Figure 10. (a) Relative hydraulic pressure gradient $\frac{S}{S_{ref}}$ and (b) hydraulic radius $\frac{R}{R_{ref}}$ as inverted from seismic observations and as shown as a function of measured relative water discharge $\frac{Q}{Q_{ref}}$. Timeseries of R and S are calculated from 5-day lowpass filtered timeseries of Q and P_w, and are then 30-day lowpass filtered (same as in Fig. 8). Timeseries of Q is 30-day lowpass filtered. Reference values for all three variables are taken as the first day of the 2017 melt-season (May 10th 2017). We compare our data to the predictions of Röthlisberger (1972) for subglacial channels evolving at equilibrium with Q (green lines, $S \propto Q^{-2/11}$ and $R \propto Q^{9/22}$) and for subglacial channels evolving through hydraulic pressure gradient changes only (blue lines, $S \propto Q^2$ and $\frac{\delta R}{\delta Q} = 0$). Arrows show the direction of time. Blue shaded areas represent the period when Q is lower than 1 m^3.s^{-1}. Line sections without the black edges show interpolated values of R and S using a cubic spline interpolation as in Fig. 8.

6   Discussion

6.1   Evaluating potential bias from changes in the number and position(s) of channel(s)

As stated in Sect. 2, the subglacial channel-flow-induced seismic power P_w depends on the number of subglacial channels
455   N (Eqs.(10) and (11)) and on the source-to-station distance, which we both considered as constant in our analysis. Here we discuss how much potential changes in N and in channel(s) positions may bias our inversions of S and R. On one hand, given the glacier configuration in our study area (250 m thick, 500 m wide Fig. 2(a)), channels-to-seismic station distance is similar regardless of whether channels are located at the glacier center or on its sides. Therefore, we do not expect changes in channel spatial positions to bias our inverted values of R and S. On the other hand, we estimate how much the observed changes in P_w
460   would require changes in N if they were to be explained only by an evolving number of channels rather than evolving S or R. From Eq.(10) we have that S weakly depends on N compared to on P_w and on water discharge Q. As a result, explaining the measured variations of P_w while imposing S constant would require N to change by more than 4 orders of magnitude ($5^{41/6}$), which is unrealistic. From Eq.(11) we have that R weakly depends on N compared to on Q. As a result, explaining P_w variations while imposing R as constant would require N to change by more than factor of 30 ($4^{-82/33}$), which is also likely
465   unrealistic since at the onset of the melt season channels are expected to form an arterial network with few channels being kept over summer (Schoof, 2010; Werder et al., 2013). Therefore, we do not expect potential changes neither in channel positions nor in N to cause significant bias in our inverted values of R and S.

6.2 Implications for inferring water discharge using seismic noise

As opposed to Gimbert et al. (2016) who inferred little variations in hydraulic pressure gradient over its two-month long period of survey on the Mendenhall Glacier, on Glacier d'Argentière we infer high and sustained channel pressurization over the whole summer and early fall (June-October). This has implications for the physics of subglacial channels, which we further discuss in Sect. 6.3, and also for our capacity to invert for discharge Q based on observed seismic power P. If one considers the equilibrium assumption over the melt season this yields, under Röthlisberger (1972) steady-state equilibrium assumptions, to the scaling $Q \propto P_w^{33/31}$ (see Eqs.(6) and (12)). When applied over the melt season using our observations of P_w at Glacier d'Argentière, this underestimates the measured discharge by more than 65%. As shown in Fig. 10, such assumption is only valid for the early and late melt season when both discharge and its variability are low. Using the approximation $Q \propto P_w^{33/31}$ may be more appropriate for periods of low melt water input and in settings with limited water input variability such as in Antarctica. If one now considers the empirical relationship $Q \propto P_w^{11/24}$ obtained from the period of channels being out of equilibrium (using Eq.(6) and $R \propto Q^{6/22}$, see Sect. 5.5), this leads to an uncertainty of less than 10% on the estimated water discharge over the melt season at Glacier d'Argentière. We therefore suggest that the $Q \propto P_w^{11/24}$ relationship may be preferred for inverting discharge based on seismic observations during periods of high melt water input and in settings with strong seasonal variability in water input (e.g. Alpine and Greenland glaciers).

6.3 Implications for subglacial hydrology and ice dynamics

6.3.1 Understanding channels approaching equilibrium at low subglacial water discharge

During the early melt season ($\frac{Q}{Q_{ref}} < 4$, $Q < 1$ m^3.s^{-1}; Figs. 5 and 10) channels are inferred to approach an equilibrium situation for which hydraulic pressure gradient scales weakly with changes in subglacial water discharge (Fig. 10). This behavior supports that the channel's hydraulic capacity is sufficient to accommodate water input at this time of the year. We propose that, at those times, changes in water supply occur at a rate that is lower than that at which channels adjust their hydraulic radius. During the early melt season, low rates in water input changes are likely caused by water supply from melt being highly damped by the snow cover (Marshall et al., 1994; Fleming and Clarke, 2005). During the late melt season ($\frac{Q}{Q_{ref}} < 4$; Fig. 10), the cause of low rates in water input is less clear. We suggest that such rates could be induced by englacial stored water being slowly released (Flowers and Clarke, 2002; Jansson et al., 2003). Because of the well-developed drainage system at those times, channels could also adjust faster their hydraulic radius than during the early melt season and therefore could behave at equilibrium for higher rates in water input than during the early melt season.

6.3.2 Using periods when channels approach equilibrium to estimate channel(s) size and number

Using Eqs.(6) and (8) of Hooke (1984) that predict the conditions of equilibrium for steady-state channels and assuming that total discharge is equally distributed over channels of identical geometry (R-channels), we find that in our case equilibrium is predicted if the number of channels lies between 4 and 6 (using an ice thickness of 250 m, a down-glacier surface slope of

500 5° and a total water discharge of 1 m^3.s^{-1}; see Appendix Sect. B). For a lower (resp. higher) number of channels, discharge per channel and thus channel-wall melt is higher (resp. lower) than the expected channel-wall creep, which violates the equilibrium condition. Our estimate of 4 to 6 channels is consistent with the numerical modelling results of Werder et al. (2013) of 4 to 5 dominant channels lying below the Gornerglestcher tongue (CH), a glacier which has a geometry similar to that of the tongue of Glacier d'Argentière (c. 500 m wide, c. 300 m maximum thickness). Further insights on the spatial evolution of

505 the subglacial drainage system could be gained using seismic arrays to locate the source(s) of subglacial flow-induced-seismic noise (Lindner et al., 2019).

We propose to estimate the absolute size of channels at the season initiation based on the channel number previously proposed. With 5 ± 1 channels and 1 m^3.s^{-1} equally distributed discharge, the average discharge per channel is of about 0.20 ± 0.05

510 m^3.s^{-1} (uncertainty is obtained from that on channels number). Considering that subglacial flow-induced-seismic noise is likely sensitive to water flow speed on the order of 1 m.s^{-1} (Gimbert et al., 2016) we can estimate a minimal channel cross-section area of about 0.20 ± 0.05 m^2, and a resulting channel radius of 0.35 ± 0.05 m (for semi-circular R-shaped channels). We note that absolute inversions of R and S could be done by explicitly formulating the Green function G in Eq.(1), and be compared to the present estimation using channels at equilibrium. However, this is beyond the scope of this study.

515 6.3.3 Understanding highly pressurized channels during the summer season

At water discharges higher than 1 m^3.s^{-1} (Fig. 5(b)) and relative changes in water discharge Q higher than 4 ($\frac{Q}{Q_{ref}}$ >4; Figs. 8 and 10)) the hydraulic pressure gradient S in channels remains high (Fig. 10). Considering that bed slope is constant, these high S-values require channels to be full and pressurized. During these periods of high discharge, as S increases with relative changes in Q (Fig. 10(a)) channels respond to changes in discharge in the same way as theoretically expected for cavities but

520 not for channels by Schoof (2010). Such an behaviour is therefore opposed to the theoretical steady-state predictions of Schoof (2010) and Werder et al. (2013) that instead support that channels have a water pressure decreasing as they develop over the summer.

Using Hooke (1984) and our estimate of 5 channels made in Sect. 6.3.2, we find that in our case channel-wall melt (i.e.

525 opening rate) is expected to dominate ice creep (i.e. closing rate) for $Q > 1$ m^3.s^{-1} (see Sect. B for details on the calculation). At steady-state this should either lead to channel growth and/or to an abrupt decrease in S down to free-flow situation (i.e. atmospheric pressure). These two scenarii are not observed during summer since R stays mainly constant (i.e. limited channel growth) and S presents high values supporting closed-flow over hourly timescales. We propose that the summer channel pressurization (high S) is due to channels responding to marked diurnal and short-term changes in water supply (as theoretically

530 described in Schoof (2010)), and that channels behave out-of-equilibrium because changes in water input occur at a rate that is higher than that at which channels can adjust their hydraulic radius.

This interpretation is supported by our diurnal analysis on R and S evolution. In the morning, S is inferred to rise earlier than R (Fig.9), suggesting that channel-wall melt does not accommodate the increase of Q fast enough and causes pressurized flow. As water supply increases, channels start to respond to the water input and grow by channel-wall melt leading to a delayed hydraulic radius R increases compared to S (Fig. 9). At the same time the channel capacity increases with R (Röthlisberger, 1972) leading to a decrease in S before Q reaches a maximum as shown in Fig. 9. During the afternoon, as the water supply decreases, R slowly decreases by much less than a percent per hour (Fig. 9). At this rate, ice creep is capable to adjust changes in R fast enough in order to limit open channel-flow (Fig. S6). This could explain why S does not show an abrupt decreases down to the early melt season values as one would expect if open channel-flow occurs (Fig. 9). The hydraulic pressure gradient therefore builds up from day-to-day over the summer. During night-time, as Q is at its minimum, the closure rate still adjusts channel size and therefore allows R to remain nearly constant through summer. This proposed scenario is consistent with both the investigated diurnal dynamics in the hydraulic properties and may explain the unexpected pressurized channels during summer. Estimation of melt and creep rates calculated from Hooke (1984) in a similar manner as in Sect. 6.3.2 supports the plausibility of such diurnal dynamics (see Appendix Sect. B for details). Further measurements remain to be conducted on glaciers with different geometries (e.g. flatter), different bed conditions (e.g soft bed glaciers) and different spatialization of water input (e.g. discrete water input through moulins) to evaluate the effect of such parameters on the subglacial hydrology dynamics. For instance, it is possible that our proposed channel's dynamic is limited to hard-bedded glaciers as soft-bedded glaciers have the capacity to store water and possibly damper the pronounced short term variability in water supply. In such setup, sediment erosion would complement ice wall melt and allow channels to be kept a much lower hydraulic pressure gradient than described in our study.

6.3.4   Channel dynamics, cavity water pressure and basal sliding

Our observations and subsequent analysis (Figs. 8 and 10) indicate that over the summer channels are pressurized and behave out-of-equilibrium. On the other hand, during summer the glacier sliding speed remain high, especially in 2018, (Fig. 5), which shows that the average basal water pressure (which is mainly set by pressure in cavities) is also high. These concomitantly high pressures in channels and in cavities suggest that the two systems may be well connected.

During summer, because of channel-flow pressurization, the channel-system does not operate under a significantly lower hydraulic potential than that of the cavity-system. This would therefore prevent significant water flow from cavities to channels, and leads to cavities that are kept pressurized. This sustained high water pressure at the glacier basis favors high glacier sliding speed over summer. Such channel-cavity-sliding link, has been previously suggested (Hubbard and Nienow, 1997; Andrews et al., 2014; Rada and Schoof, 2018) but was not based on an independent analysis of the cavities and channels hydraulic conditions as we propose here through combining seismic and basal sliding speed measurements.

We suggest that during these periods of pronounced short-term variability in water supply, the whole drainage system becomes well-connected although with a limited drainage capacity. Thus the channel system may participate in maintaining high pressure in cavities and thus high sliding speed during periods of high water supply variability. Short-term variability in water supply may lead to pronounced glacier acceleration even during situations of a well-developed channel network. Such subglacial hydrology/ice dynamics link deserves further investigation through combination of seismic observations and subglacial hydrology/ice dynamics models (e.g. Gagliardini and Werder, 2018). Indeed a better understanding of the impact of short-lived water input on glacier dynamics is necessary as under climate warming short-term climatic variability and extreme event occurrences are expected to increase (Hynčica and Huth, 2019), potentially causing greater glacier acceleration than previously thought (e.g. Tedstone et al., 2015).

7 Conclusions

We investigate the physics of subglacial channels and its link with basal sliding beneath an Alpine glacier (Glacier d'Argentière, French Alps) through the analysis of a unique two-year long dataset made of on-ice measured subglacial water-flow-induced seismic power and in-situ measured glacier basal sliding speed. Our study shows that the theory of Gimbert et al. (2016) is consistent with our observations and that the analysis of the seismic power measured within the [3-7] Hz frequency range allows to study the subglacial drainage properties over a complete melt season and down to diurnal timescales.

We quantify temporal changes in channels' hydraulic radius and hydraulic pressure gradient using the theory of Gimbert et al. (2016) and measurements of water discharge concomitant to our seismic record. Our approach allows to isolate subglacial water-flow-induced seismic power from that of other seismic sources, and makes possible observing changes at various timescales (from seasonal to hourly) and water discharge ranges (from 0.25 to 10 $\mathrm{m}^3.\mathrm{sec}^{-1}$). At seasonal timescales we support, for the first time, that hydraulic radius and hydraulic pressure gradient both present at least a two-fold increase from spring to summer, followed by a comparable decrease towards autumn. Comparing our analysis to the theoretical predictions of Röthlisberger (1972) we identify that channel dynamics over the season is characterized by two distinct regimes yet unprecedentedly reported. At low discharge during the early and late melt season our analysis supports that channels respond to changes in discharge mainly through changes in hydraulic radius, and that the strong changes in hydraulic radius and weak changes in pressure gradient are similar to those predicted by theory for channels behaving at equilibrium. We propose that, at those times, changes in water input occur at a rate that is lower than that at which channels adjust their hydraulic radius. During the early melt season, these low rates in water input changes are likely caused by water supply from melt being highly damped by the snow cover. From this equilibrium channel-dynamics condition we are able to estimate the number of channels, which we find to be between 4 to 6, each channel having a radius of about 0.5 m in the early melt season that may go up to 2 m in summer. At high discharge and high short-term water-supply variability (often during summertime) we show that channels undergo strong changes in hydraulic pressure gradient, a behavior that is not expected for channels at equilibrium. Instead, those changes in hydraulic pressure gradient are well reproduced by theory under the end-member consideration of no changes

in channel geometry in response to changes in water input. We propose that, at those times, channels behave out-of-equilibrium because changes in water input occur at a rate that is much higher than that at which channels adjust their hydraulic radius. This interpretation is supported by R and S behaviors at the diurnal scale, which show that channels pressurize in the early morning and depressurize in the afternoon as their hydraulic radius slowly grow concomitantly with the water supply rise. At night when water discharge decreases, ice creep then allows channels to recover their initial early morning hydraulic radius. We do not capture significant decrease of the hydraulic pressure gradient during those days, which indicates that the hydraulic pressure gradient builds up from day-to-day concomitantly to a hydraulic radius that is kept nearly constant. Channels may thus remain pressurized over the whole summer because of the short-term (diurnal, rain) variability in water supply, which forces channels to respond through a transient-dynamic state. We expect our analysis of subglacial hydrology to be applicable to glaciers of similar geometry (relatively steep U-shaped valley glaciers) and similar highly variable and distributed water supply than those of Glacier d'Argentière.

Channels behaving out-of-equilibrium during most of the melt season also has implications for the use of subglacial water-flow-induced seismic power P_w to invert for water discharge Q. The empirical relationship between Q and P_w that we derive during the period when channels are out-of-equilibrium allows estimating a water discharge from seismic noise with an error of less than 10 %, while an error of 65 % is obtained when assuming channels at equilibrium. Our presently proposed out-of-equilibrium relationship for inverting discharge could be applied in settings with strong seasonal variability in water supply (e.g. Alpine and Greenland glaciers). During summer we also observe high and sustained basal sliding, supporting that the widespread inefficient drainage system (cavities) is likely pressurized. We propose that channels being also pressurized may help sustain high pressure in cavities and thus high glacier sliding speed.

These results demonstrate that on-ice passive seismology is an efficient tool to overcome the classical observational limitations faced when investigating subglacial hydrology processes. In this respect, our results bring new constraints on channels physics, on links between channels, cavities and sliding, and on the use of passive seismology to invert for subglacial water discharge. In the future, an essential step towards strengthening our knowledge on the physics of subglacial processes would be to assess the applicability of our findings over a wider range of glacier geometries (e.g. soft bed glaciers and ice sheets) both through extended on-site seismic survey and the use of our seismically-derived observations as constraints for subglacial hydrology/ice dynamics models.

Code and data availability. Timeseries of of physical quantities shown in Figs. 5 and 8 can be found at https://doi.org/10.5281/zenodo. 3701520 (Nanni et al., 2020). The complete dataset will be made publicly available in the future. Ongoing work is taking place to meet the format and documentation required for the release for the complete seismic survey, which is expected to happen fully or partially by mid-2021. In the meantime, it is available on request from the corresponding author. The Python and SAC codes for seismic power calculation are given in the Supplementary Materials.

Appendix A: Frequency content of the water discharge and the subglacial channel-flow-induced seismic power

We show in Fig. A1 the power spectrum of the water discharge Q (blue lines) and subglacial channel-flow-induced seismic power P_w as a function of the period. We observe for both variables a well-defined peak at one day and 12 h period. This shows that these signals present a clear diurnal and sub-diurnal variability, and supports our choice to band-pass-filter these signals within [6-36] h to study these short-term variabilities.
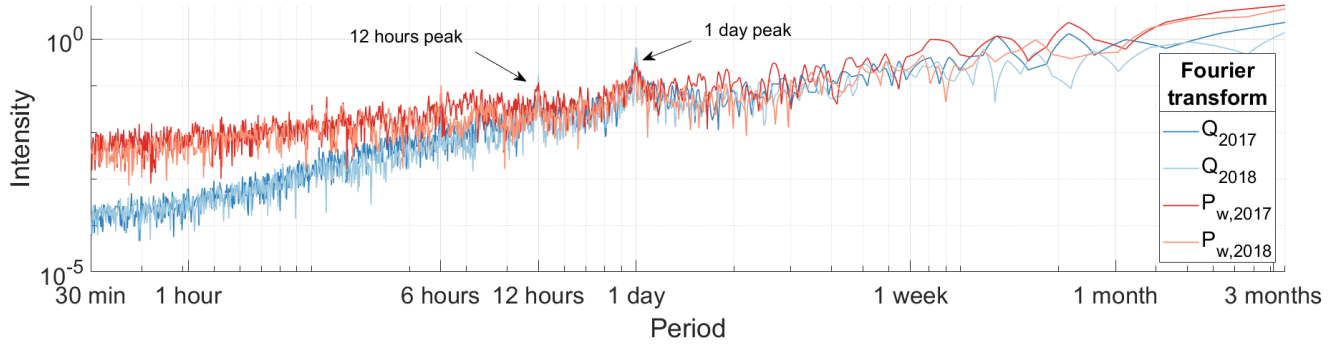
Figure A1. Power spectrum of the water discharge Q (blue lines) and subglacial channel-flow-induced seismic power P_w (red lines) shown a function of the period. Both axis are in logarithmic scale (1 over the frequency.)

Appendix B: Evaluating theoretical melt and creep rates with Hooke (1984)' equations

We used in this study the equations 6 and 8 of Hooke (1984) to evaluate the theoretical melt rate $\dot{m}$ and creep rate $\dot{r}$, as follows

$$\dot{m} = C_2 Q^{3/5} sin(\beta)^{6/5}, \tag{B1}$$

$$\dot{r} = C_3 \frac{Q^{2/5}}{sin(\beta)^{1/5}} H^3, \tag{B2}$$

with H the ice thickness, β the down-glacier surface slope, C_2 and C_3 constant. We use the values of Hooke (1984) for the two constants: $C_2 = 3.731e^{-5}$ m$^{-4/5}$ s$^{-2/3}$ and $C_2 = 5.71e^{-14}$ m$^{-16/5}$ s$^{-3/5}$. For the glacier geometry we use using an ice thickness of 250 m and a down-glacier surface slope of 5°.

Appendix C: Notations

Author contributions. U.N., F.G. and C.V. designed the study. U.N. performed the seismic analysis with input from F.G. and F.W.. U.N. interpreted the results with input from F.G.. U.N. led the writing of the paper and F.G., C.V., F. W. and D. G. contributed to it. L.P and L.M were in charge of the basal sliding speed measurements. All authors participated to field installations.

Competing interests. The authors declare that they have no competing interests.

Acknowledgements. We thank J. Bolibar, C. Bouchayer, J. Brives, J. Brondex, J. Chowdhry, S. Escalle, A. Gilbert, B. Jourdain, O. Laarman, B. Lipovsky, N. Maier, A. Palenstijn, O. Passalacqua, L. Preiswerk, A. Rabatel, V. Ramseyer, V. Tsai, B. Urruty and J. Wille for assistance in the field. We are indebted to Electricité Emosson SA (hydroelectric company) for the water discharge measurements and access to the subglacial galleries and the French GLACIOCLIM project for temperature and precipitation data (https://glacioclim.osug.fr/). We thank Nikos Germenis for technical support on the ARG seismic network (https://geobit-instruments.com/). U. Nanni would like to thank J. Bolibar, B. de Fleurian and L. Preiswerk for fruitful discussions. This work was supported by the SEISMORIV project (ANR-17-CE01-0008) and the SAUSSURE project (ANR-18-CE01-0015) funded by the Agence National de la Recherche (ANR). U. Nanni is funded by the French Ministère de l'Enseignement Supérieur, de la Recherche et de l'Innovation (MESRI).

References

Aki, K. and Richards, P. G.: Quantitative seismology, 2002.

Allstadt, K. and Malone, S. D.: Swarms of repeating stick-slip icequakes triggered by snow loading at Mount Rainier volcano, Journal of Geophysical Research: Earth Surface, 119, 1180–1203, 2014.

Anderson, S. P., Longacre, S. A., and Kraal, E. R.: Patterns of water chemistry and discharge in the glacier-fed Kennicott River, Alaska: evidence for subglacial water storage cycles, Chemical Geology, 202, 297–312, 2003.

Andrews, L. C., Catania, G. A., Hoffman, M. J., Gulley, J. D., Lüthi, M. P., Ryser, C., Hawley, R. L., and Neumann, T. A.: Direct observations of evolving subglacial drainage beneath the Greenland Ice Sheet, Nature, 514, 80, 2014.

Bartholomaus, T. C., Anderson, R. S., and Anderson, S. P.: Response of glacier basal motion to transient water storage, Nature Geoscience, 1, 33, 2008.

Bartholomaus, T. C., Anderson, R. S., and Anderson, S. P.: Growth and collapse of the distributed subglacial hydrologic system of Kennicott Glacier, Alaska, USA, and its effects on basal motion, Journal of Glaciology, 57, 985–1002, 2011.

Bartholomaus, T. C., Amundson, J. M., Walter, J. I., O'Neel, S., West, M. E., and Larsen, C. F.: Subglacial discharge at tidewater glaciers revealed by seismic tremor, Geophysical research letters, 42, 6391–6398, 2015.

Bartholomew, I., Nienow, P., Mair, D., Hubbard, A., King, M. A., and Sole, A.: Seasonal evolution of subglacial drainage and acceleration in a Greenland outlet glacier, Nature Geoscience, 3, 408–411, 2010.

Brondex, J., Gagliardini, O., Gillet-Chaulet, F., and Durand, G.: Sensitivity of grounding line dynamics to the choice of the friction law, Journal of Glaciology, 63, 854–866, 2017.

Burtin, A., Bollinger, L., Vergne, J., Cattin, R., and Nábělek, J.: Spectral analysis of seismic noise induced by rivers: A new tool to monitor spatiotemporal changes in stream hydrodynamics, Journal of Geophysical Research: Solid Earth, 113, 2008.

Burtin, A., Cattin, R., Bollinger, L., Vergne, J., Steer, P., Robert, A., Findling, N., and Tiberi, C.: Towards the hydrologic and bed load monitoring from high-frequency seismic noise in a braided river: The "torrent de St Pierre", French Alps, Journal of hydrology, 408, 43–53, 2011.

Chandler, D., Wadham, J., Lis, G., Cowton, T., Sole, A., Bartholomew, I., Telling, J., Nienow, P., Bagshaw, E., Mair, D., et al.: Evolution of the subglacial drainage system beneath the Greenland Ice Sheet revealed by tracers, Nature Geoscience, 6, 195, 2013.

Church, G., Bauder, A., Grab, M., Rabenstein, L., Singh, S., and Maurer, H.: Detecting and characterising an englacial conduit network within a temperate Swiss glacier using active seismic, ground penetrating radar and borehole analysis, Annals of Glaciology, pp. 1–13, 2019.

Collins, D. N.: Quantitative determination of the subglacial hydrology of two Alpine glaciers, Journal of Glaciology, 23, 347–362, 1979.

Copland, L., Harbor, J., and Sharp, M.: Borehole video observation of englacial and basal ice conditions in a temperate valley glacier, Annals of Glaciology, 24, 277–282, 1997.

de Fleurian, B., Werder, M. A., Beyer, S., Brinkerhoff, D. J., Delaney, I., Dow, C. F., Downs, J., Gagliardini, O., Hoffman, M. J., Hooke, R. L., et al.: SHMIP The subglacial hydrology model intercomparison Project, Journal of Glaciology, 64, 897–916, 2018.

Doyle, S. H., Hubbard, A., Fitzpatrick, A. A., As, D., Mikkelsen, A. B., Pettersson, R., and Hubbard, B.: Persistent flow acceleration within the interior of the Greenland ice sheet, Geophysical Research Letters, 41, 899–905, 2014.

Fleming, S. W. and Clarke, G. K.: Attenuation of high-frequency interannual streamflow variability by watershed glacial cover, Journal of Hydraulic Engineering, 131, 615–618, 2005.

Flowers, G. E.: Modelling water flow under glaciers and ice sheets, Proceedings of the Royal Society A: Mathematical, Physical and Engineering Sciences, 471, 20140 907, 2015.

Flowers, G. E. and Clarke, G. K.: A multicomponent coupled model of glacier hydrology 1. Theory and synthetic examples, Journal of Geophysical Research: Solid Earth, 107, ECV–9, 2002.

Fountain, A. G. and Walder, J. S.: Water flow through temperate glaciers, Reviews of Geophysics, 36, 299–328, 1998.

Gagliardini, O. and Werder, M. A.: Influence of increasing surface melt over decadal timescales on land-terminating Greenland-type outlet glaciers, Journal of Glaciology, 64, 700–710, 2018.

Gagliardini, O., Cohen, D., Råback, P., and Zwinger, T.: Finite-element modeling of subglacial cavities and related friction law, Journal of Geophysical Research: Earth Surface, 112, 2007.

Gimbert, F., Tsai, V. C., and Lamb, M. P.: A physical model for seismic noise generation by turbulent flow in rivers, Journal of Geophysical Research: Earth Surface, 119, 2209–2238, 2014.

Gimbert, F., Tsai, V. C., Amundson, J. M., Bartholomaus, T. C., and Walter, J. I.: Subseasonal changes observed in subglacial channel pressure, size, and sediment transport, Geophysical Research Letters, 43, 3786–3794, 2016.

Gräff, D., Walter, F., and Lipovsky, B. P.: Crack wave resonances within the basal water layer, Annals of Glaciology, pp. 1–9, 2019.

Hantz, D. and Lliboutry, L.: Waterways, ice permeability at depth, and water pressures at Glacier d'Argentiere, French Alps, Journal of glaciology, 29, 227–239, 1983.

Hewitt, I.: Seasonal changes in ice sheet motion due to melt water lubrication, Earth and Planetary Science Letters, 371, 16–25, 2013.

Hoffman, M. J., Andrews, L. C., Price, S. F., Catania, G. A., Neumann, T. A., Lüthi, M. P., Gulley, J., Ryser, C., Hawley, R. L., and Morriss, B.: Greenland subglacial drainage evolution regulated by weakly connected regions of the bed, Nature communications, 7, 13 903, 2016.

Hooke, R. L.: On the role of mechanical energy in maintaining subglacial water conduits at atmospheric pressure, Journal of Glaciology, 30, 180–187, 1984.

Hooke, R. L., Wold, B., and Hagen, J. O.: Subglacial hydrology and sediment transport at Bondhusbreen, southwest Norway, Geological Society of America Bulletin, 96, 388–397, 1985.

Hubbard, B. and Nienow, P.: Alpine subglacial hydrology, Quaternary Science Reviews, 16, 939–955, 1997.

Hynčica, M. and Huth, R.: Long-term changes in precipitation phase in Europe in cold half year, Atmospheric Research, 227, 79–88, 2019.

Iken, A. and Bindschadler, R. A.: Combined measurements of subglacial water pressure and surface velocity of Findelengletscher, Switzerland: conclusions about drainage system and sliding mechanism, Journal of Glaciology, 32, 101–119, 1986.

Iken, A. and Truffe, M.: The relationship between subglacial water pressure and velocity of Findelengletscher, Switzerland, during its advance and retreat, Journal of Glaciology, 43, 328–338, 1997.

Jansson, P., Hock, R., and Schneider, T.: The concept of glacier storage: a review, Journal of Hydrology, 282, 116–129, 2003.

Joughin, I., Smith, B. E., and Howat, I.: Greenland Ice Mapping Project: ice flow velocity variation at sub-monthly to decadal timescales., Cryosphere, 12, 2018.

Lindner, F., Walter, F., Laske, G., and Gimbert, F.: Glaciohydraulic seismic tremors on an Alpine glacier, The Cryosphere Discuss, 10, 2019.

Lliboutry, L.: General theory of subglacial cavitation and sliding of temperate glaciers, Journal of Glaciology, 7, 21–58, 1968.

Manning, R., Griffith, J. P., Pigot, T., and Vernon-Harcourt, L. F.: On the flow of water in open channels and pipes, Ireland, 1890.

Marshall, S., Roads, J. O., and Glatzmaier, G.: Snow hydrology in a general circulation model, Journal of Climate, 7, 1251–1269, 1994.

730 Nanni, U., Gimbert, F., Vincent, C., Gräff, D., Walter, F., Piard, L., and Moreau, L.: DATA of 'Quantification of seasonal and diurnal dynamics of subglacial channels using seismic observations on an Alpine Glacier.' from Nanni et al. 2020,, https://doi.org/10.5281/zenodo.3701520, https://doi.org/10.5281/zenodo.3701520, Datastet associated to the present study, 2020.

Nienow, P., Sharp, M., and Willis, I.: Seasonal changes in the morphology of the subglacial drainage system, Haut Glacier d'Arolla, Switzerland, Earth Surface Processes and Landforms, 23, 825–843, 1998.

735 Nienow, P., Hubbard, A., Hubbard, B., Chandler, D., Mair, D. W. F., Sharp, M., and Willis, I.: Hydrological controls on diurnal ice flow variability in valley glaciers, Journal of Geophysical Research: Earth Surface, 110, 2005.

Nienow, P. W., Sharp, M., and Willis, I. C.: Velocity–discharge relationships derived from dye tracer experiments in glacial meltwaters: implications for subglacial flow conditions, Hydrological Processes, 10, 1411–1426, 1996.

Nye, J.: Water flow in glaciers: jökulhlaups, tunnels and veins, Journal of Glaciology, 17, 181–207, 1976.

740 Palmer, S., Shepherd, A., Nienow, P., and Joughin, I.: Seasonal speedup of the Greenland Ice Sheet linked to routing of surface water, Earth and Planetary Science Letters, 302, 423–428, 2011.

Parizek, B. R. and Alley, R. B.: Implications of increased Greenland surface melt under global-warming scenarios: ice-sheet simulations, Quaternary Science Reviews, 23, 1013–1027, 2004.

Preiswerk, L. E. and Walter, F.: High-Frequency (> 2 Hz) Ambient Seismic Noise on High-Melt Glaciers: Green's Function Estimation and
745 Source Characterization, Journal of Geophysical Research: Earth Surface, 123, 1667–1681, 2018.

Rada, C. and Schoof, C.: Channelized, distributed, and disconnected: subglacial drainage under a valley glacier in the Yukon., Cryosphere, 12, 2018.

Richards, K., Sharp, M., Arnold, N., Gurnell, A., Clark, M., Tranter, M., Nienow, P., Brown, G., Willis, I., and Lawson, W.: An integrated approach to modelling hydrology and water quality in glacierized catchments, Hydrological Processes, 10, 479–508, 1996.

750 Roth, D. L., Brodsky, E. E., Finnegan, N. J., Rickenmann, D., Turowski, J. M., and Badoux, A.: Bed load sediment transport inferred from seismic signals near a river, Journal of Geophysical Research: Earth Surface, 121, 725–747, 2016.

Röthlisberger, H.: Water pressure in intra-and subglacial channels, Journal of Glaciology, 11, 177–203, 1972.

Schmandt, B., Aster, R. C., Scherler, D., Tsai, V. C., and Karlstrom, K.: Multiple fluvial processes detected by riverside seismic and infrasound monitoring of a controlled flood in the Grand Canyon, Geophysical Research Letters, 40, 4858–4863, 2013.

755 Schoof, C.: The effect of cavitation on glacier sliding, in: Proceedings of the Royal Society of London A: Mathematical, Physical and Engineering Sciences, vol. 461, pp. 609–627, The Royal Society, 2005.

Schoof, C.: Ice-sheet acceleration driven by melt supply variability, Nature, 468, 803–806, 2010.

Seaberg, S. Z., Seaberg, J. Z., Hooke, R. L., and Wiberg, D. W.: Character of the englacial and subglacial drainage system in the lower part of the ablation area of Storglaciären, Sweden, as revealed by dye-trace studies, Journal of Glaciology, 34, 217–227, 1988.

760 Sole, A., Nienow, P., Bartholomew, I., Mair, D., Cowton, T., Tedstone, A., and King, M. A.: Winter motion mediates dynamic response of the Greenland Ice Sheet to warmer summers, Geophysical Research Letters, 40, 3940–3944, 2013.

Strickler, A.: Contributions to the question of a velocity formula and roughness data for streams, channels and closed pipelines, Lab. of Hydraul. and Water Resour, 1981.

Sugiyama, S., Skvarca, P., Naito, N., Enomoto, H., Tsutaki, S., Tone, K., Marinsek, S., and Aniya, M.: Ice speed of a calving glacier
765 modulated by small fluctuations in basal water pressure, Nature Geoscience, 4, 597, 2011.

Sundal, A. V., Shepherd, A., Nienow, P., Hanna, E., Palmer, S., and Huybrechts, P.: Melt-induced speed-up of Greenland ice sheet offset by efficient subglacial drainage, Nature, 469, 521, 2011.

Tedstone, A. J., Nienow, P. W., Sole, A. J., Mair, D. W., Cowton, T. R., Bartholomew, I. D., and King, M. A.: Greenland ice sheet motion insensitive to exceptional meltwater forcing, Proceedings of the National Academy of Sciences, 110, 19 719–19 724, 2013.

770 Tedstone, A. J., Nienow, P. W., Gourmelen, N., Dehecq, A., Goldberg, D., and Hanna, E.: Decadal slowdown of a land-terminating sector of the Greenland Ice Sheet despite warming, Nature, 526, 692–695, 2015.

Theakstone, W. H. and Knudsen, N. T.: Temporal changes of glacier hydrological systems indicated by isotopic and related observations at Austre Okstindbreen, Okstindan, Norway, 1976–87, Annals of Glaciology, 13, 252–256, 1989.

Tranter, M., Brown, G. H., Hodson, A. J., and Gurnell, A. M.: Hydrochemistry as an indicator of subglacial drainage system structure: a

775 comparison of alpine and sub-polar environments, Hydrological Processes, 10, 541–556, 1996.

Tranter, M., Sharp, M., Brown, G., Willis, I., Hubbard, B., Nielsen, M., Smart, C., Gordon, S., Tulley, M., and Lamb, H.: Variability in the chemical composition of in situ subglacial meltwaters, Hydrological Processes, 11, 59–77, 1997.

Tsai, V. C., Minchew, B., Lamb, M. P., and Ampuero, J.-P.: A physical model for seismic noise generation from sediment transport in rivers, Geophysical Research Letters, 39, 2012.

780 Vincent, C. and Moreau, L.: Sliding velocity fluctuations and subglacial hydrology over the last two decades on Argentière glacier, Mont Blanc area, Journal of Glaciology, pp. 1–11, 2016.

Vincent, C., Soruco, A., Six, D., and Le Meur, E.: Glacier thickening and decay analysis from 50 years of glaciological observations performed on Glacier d'Argentière, Mont Blanc area, France, Annals of glaciology, 50, 73–79, 2009.

Vivian, R. and Bocquet, G.: Subglacial cavitation phenomena under the glacier d'Argentière, Mont Blanc, France, Journal of Glaciology, 12,

785 439–451, 1973.

Vivian, R. A. and Zumstein, J.: Hydrologie sous-glaciaire au glacier d'Argentière (Mont-Blanc, France), IASH Publ, 95, 53–64, 1973.

Walder, J. and Hallet, B.: Geometry of former subglacial water channels and cavities, Journal of Glaciology, 23, 335–346, 1979.

Welch, P.: The use of fast Fourier transform for the estimation of power spectra: a method based on time averaging over short, modified periodograms, IEEE Transactions on audio and electroacoustics, 15, 70–73, 1967.

790 Werder, M. A., Hewitt, I. J., Schoof, C. G., and Flowers, G. E.: Modeling channelized and distributed subglacial drainage in two dimensions, Journal of Geophysical Research: Earth Surface, 118, 2140–2158, 2013.

Willis, I. C., Sharp, M. J., and Richards, K. S.: Configuration of the drainage system of Midtdalsbreen, Norway, as indicated by dye-tracing experiments, Journal of Glaciology, 36, 89–101, 1990.

Zwally, H. J., Abdalati, W., Herring, T., Larson, K., Saba, J., and Steffen, K.: Surface melt-induced acceleration of Greenland ice-sheet flow,

795 Science, 297, 218–222, 2002.

Table C1. Summary of all variables, physical quantities, and mathematical functions used in the main text.

Variable/Symbol[a]	Description	Units	Reference[b]
F	Frictional force generated by turbulent water flow	N	Eq. 1
x_0	Seismic source location		Eq. 1
x	Source-to-sensor distance	m	Eq. 1
U	Ground velocity	$m.s^{-1}$	Eq. 1
t	Time	s	Sect. 2
G	Displacement Green's function		Eq. 1
T	Time period of the seismic signal	s	Eq. 2
f	Frequency of the seismic signal	Hz	Eq. 2
dt	Time duration of Welch's window to calculate seismic power	s	Sect. 4
P	Seismic power	dB[c]	Eq. 2, Figs. 4 and 3
$P_{[3\text{-}7]\,Hz}$	P as averaged within the [3-7] Hz frequency range	dB	Fig. 5
P_w	Seismic power induced by turbulent water flow	dB	Eq. 3, Figs. 3 and 9
P_A	Anthropogenic noise	dB	Sect. 4.2, Fig. 3
V_w	Water flow velocity	$m.s^{-1}$	Sect. 2
u_*	River/channel bed shear velocity	$m.s^{-1}$	Eq. 3, Fig. 1
W	Water conduit width	m	Eq. 3
H	Water flow depth	m	Eq. 3
k_s	Conduit wall roughness size	m	Eq. 3
β	Function of conduit shape and fullness		Eq. 4
n'	Manning's coefficient		Sect. 2
g	Gravitational acceleration	$m.s^{-2}$	Sect. 2
Q	Subglacial water discharge	$m.s^{-3}$	Eq. 5, Figs. 5 and 9
R	Hydraulic radius		Eq. 11
	Relative hydraulic radius from Sect. 5.4 on		Eq. 11, Figs. 8 and 9
S	Hydraulic pressure gradient		Eq. 10
	Relative hydraulic pressure gradient from Sect. 5.4 on		Eq. 10, Figs. 8 and 9
N	Number of subglacial channel(s)		Eq. 4
V	Glacier basal sliding speed	$mm.h^{-1}$	Figs. 5, 8 and 9
S_r	Anthropogenic noise quantificator		Sect. 4.2, Fig. 3
X_{day}	Any variable X bandpass filtered within [6-36] h		Eq. 15, Figs. 9 and 7
$(X_{day})_{max}$	Daily maximum of a given variable X	dB	Eq. 17
$\delta t_{Q,X}$	Time lag between $(Q_{day})_{max}$ and $(X_{day})_{max}$	h	Eq. 17, Figs. 9 and 7
$C_v(X)$	Coefficient of diurnal variation of a given variable X	%	Eq. 15, Fig. 9
$(P_{w,day})_{rising}$	P_w during the daily increase in Q	dB	Eq. 16
$(P_{w,day})_{falling}$	P_w during the daily decrease in Q	dB	Eq. 16
ϕ	Daily hysteresis between P_w and Q		Eq. 16, Fig. 7
X_{ref}	Reference state of a given variable X at a reference time		Eqs. 10 and 11 Figs. 6, 7, 8, 9 and 10

(a) First section lists variables characterizing the propagation of seismic wave, second section lists variables characterizing the seismic power properties, third section lists variables and constants related the physical properties of river flow, fourth section lists variables characterizing the hydraulic and glaciological properties of the subglacial drainage system and fifth section lists the indicators defined to investigate subglacial water flow properties.
(b) Relevant occurrences in the main text of the variables, physical quantities, and mathematical functions.
(c) Decimal logarithmic relative to $(m.s^{-1})^2.Hz^{-1}$.